

# Explicit algebraic subgrid stress models with application to rotating channel flow

LINUS MARSTORP, GEERT BRETHOUWER†, OLOF GRUNDESTAM AND ARNE V. JOHANSSON

Linné Flow Centre, Department of Mechanics, KTH, SE-100 44 Stockholm, Sweden

(Received 31 January 2008; revised 3 July 2009; accepted 3 July 2009; first published online 12 October 2009)

New explicit subgrid stress models are proposed involving the strain rate and rotation rate tensor, which can account for rotation in a natural way. The new models are based on the same methodology that leads to the explicit algebraic Reynolds stress model formulation for Reynolds-averaged Navier–Stokes simulations. One dynamic model and one non-dynamic model are proposed. The non-dynamic model represents a computationally efficient subgrid scale (SGS) stress model, whereas the dynamic model is the most accurate. The models are validated through large eddy simulations (LESs) of spanwise and streamwise rotating channel flow and are compared with the standard and dynamic Smagorinsky models. The proposed explicit dependence on the system rotation improves the description of the mean velocity profiles and the turbulent kinetic energy at high rotation rates. Comparison with the dynamic Smagorinsky model shows that not using the eddy-viscosity assumption improves the description of both the Reynolds stress anisotropy and the SGS stress anisotropy. LESs of rotating channel flow at  $Re_\tau = 950$  have been carried out as well. These reveal some significant Reynolds number influences on the turbulence statistics. LESs of non-rotating turbulent channel flow at  $Re_\tau = 950$  show that the new explicit model especially at coarse resolutions significantly better predicts the mean velocity, wall shear and Reynolds stresses than the dynamic Smagorinsky model, which is probably the result of a better prediction of the anisotropy of the subgrid dissipation.

---

## 1. Introduction

Subgrid scale (SGS) stress models based on the eddy-viscosity assumption, such as the widely known Smagorinsky model, are popular in large eddy simulations (LESs). They are simple and robust and are able to provide for a fairly correct amount of energy dissipation, at least with a dynamic determination of the model constant. A correct description of the mean energy drain is in many cases sufficient to obtain a good description of the resolved scales in LES. However, improvements in comparison with eddy-viscosity models have been reported with various kinds of mixed models, where the eddy-viscosity term is accompanied with a second term which is not aligned with the resolved rate of strain. In the mixed-similarity model, originally proposed by Bardina, Ferziger & Reynolds (1983), the Smagorinsky model is combined with a scale-similarity term computed using explicit filtering assuming scale invariance of the SGS stress. Several authors have reported that the mixed-similarity model is superior to the Smagorinsky model. For example Vreman, Geurts & Kuerten

† Email address for correspondence: geert@mech.kth.se

(1994) showed that the dynamic mixed-similarity model outperforms the dynamic Smagorinsky model in LES of a temporal mixing layer. The Clark model (Clark, Ferziger & Reynolds 1979), or tensor eddy-viscosity model, is a computationally efficient alternative to the scale-similarity model part. It can be considered to be a first-order approximation of the scale-similarity model. The models proposed in this paper depend explicitly on the resolved strain rate and rotation rate tensors and consist of two terms: an eddy-viscosity term that provides for dissipation of energy and a nonlinear term that accounts for subgrid stress anisotropy and thereby improves the description of the individual SGS stresses. In that respect the new explicit models belong to the group of mixed SGS models.

Explicit algebraic Reynolds stress models (EARSMS), whereby the Reynolds stress anisotropy is described in terms of the mean strain rate and the mean rotation rate tensors, are popular in the Reynolds-averaged Navier–Stokes (RANS) community. A recent example is the EARSMS by Wallin & Johansson (2000). It is based on a modelled transport equation of the Reynolds stresses and on the assumption that the advection and diffusion of the Reynolds stress anisotropy are negligible. The EARSMS can correctly account for rotation and has been shown to be superior to classical eddy-viscosity-based models, especially regarding the description of rotating flows. Explicit SGS stress models for LES based on polynomials of the resolved strain rate and the resolved rotation rate tensors have been proposed by Lund & Nikov (1992), Meneveau, Lund & Moin (1992) and Wong (1992). A recent example is the nonlinear dynamic SGS stress model by Wang & Bergstrom (2005), which consists of three base tensors and three dynamic coefficients. One of the terms in the model is similar to the dynamic Smagorinsky model. Wang & Bergstrom (2005) showed that the dynamic nonlinear model predicts a more realistic tensorial alignment of the SGS stress than eddy-viscosity models and can provide for backscatter without clipping or averaging of the dynamic model parameters.

LESs of rotating turbulent flows put high demands on the SGS model. In spanwise rotating channel flow, rapid rotation can result in an almost laminar flow at the stabilized side of the channel, as shown by the direct numerical simulations (DNSs; Kristoffersen & Andersson 1993), implying vanishing SGS stresses. The flow can even become fully laminar at very rapid rotation rates (Grundestam, Wallin & Johansson 2008). Rotation can also promote growth of fluctuations in a certain direction, resulting in very anisotropic SGS stresses.

LES of rotating channel flow has been used as a test case for validation of SGS models in some studies. Lamballais, Métais & Lesieur (1998) validated their dynamic spectral eddy-viscosity model through LES of spanwise rotating channel flow. Also Tsubokura *et al.* (1999) used spanwise rotating channel flow to investigate the performance of different SGS stress models. Oberlack *et al.* (2006) performed DNSs, LESs and RANS simulations of streamwise rotating channel flow and showed that the dynamic Smagorinsky model did not work very well in that case.

The objective of this study is to develop new models for the SGS stress by applying the same kind of methodology that leads to the EARSMS for RANS mode. A dynamic model and a computationally more efficient non-dynamic model are proposed. The idea is that these new models can improve the description of the SGS anisotropy compared to eddy-viscosity models. Since the new models can include the effect of system rotation in a natural way they have a particular potential for rotating flows.

In this paper, we validate the explicit SGS models in spanwise rotating turbulent channel flow, since this is a challenging problem for LES. The SGS stresses become very anisotropic and a correct description of the SGS stress anisotropy cannot be

obtained with a simple eddy-viscosity model. Moreover the stabilizing/destabilizing effects of rotation have to be captured by the SGS model. The SGS model has to reduce the SGS dissipation at the stabilized side of the channel in order to capture the physics of the flow. We also validate the model in streamwise rotating channel flow, which is also a challenging test case for LES, as shown by Oberlack *et al.* (2006). LES of non-rotating and rotating channel flows at relatively high Reynolds number are carried out in order to explore Reynolds number effects on the turbulence and sensitivity of the LES to grid resolution.

## 2. Explicit algebraic subgrid stress models

The transport equation for the SGS stress tensor  $\tau_{ij} = (\widetilde{u_i u_j} - \widetilde{u_i} \widetilde{u_j})$ , where  $\widetilde{\cdot}$  denotes a homogeneous filter operator, can be written in the same way as the transport equation for the Reynolds stress (see Germano 1992). Analogous to the Reynolds stress anisotropy tensor we define the SGS stress anisotropy tensor as

$$a_{ij} = \frac{\tau_{ij}}{K_{SGS}} - \frac{2}{3}\delta_{ij}, \quad (2.1)$$

where  $K_{SGS} = (\widetilde{u_i u_i} - \widetilde{u_i} \widetilde{u_i})/2$  is the SGS kinetic energy. In a non-rotating frame the transport equation for  $a_{ij}$  reads

$$K_{SGS} \frac{Da_{ij}}{Dt} - \left( \frac{\partial D_{ijk}^{\tau_{ij}}}{\partial x_k} - \frac{\tau_{ij}}{K_{SGS}} \frac{\partial D_k^{K_{SGS}}}{\partial x_k} \right) = -\frac{\tau_{ij}}{K_{SGS}} (P - \epsilon) + P_{ij} - \epsilon_{ij} + \Pi_{ij}, \quad (2.2)$$

where

$$\begin{aligned} -D_{ijk}^{\tau_{ij}} = & -(u_i \widetilde{u_j} u_k - \widetilde{u_i} (\widetilde{u_j} u_k - \widetilde{u_j} \widetilde{u_k}) - \widetilde{u_j} (\widetilde{u_k} u_i - \widetilde{u_k} \widetilde{u_i}) - \widetilde{u_k} (\widetilde{u_i} u_j - \widetilde{u_i} \widetilde{u_j}) - \widetilde{u_i} \widetilde{u_j} \widetilde{u_k} \\ & + \frac{1}{\rho} (\widetilde{p} u_i - \widetilde{p} \widetilde{u_i}) \delta_{jk} + \frac{1}{\rho} (\widetilde{p} u_j - \widetilde{p} \widetilde{u_j}) \delta_{ik} - \nu \frac{\partial}{\partial x_k} (\widetilde{u_i} u_j - \widetilde{u_i} \widetilde{u_j})) \end{aligned} \quad (2.3)$$

and  $-D_k^{K_{SGS}} = -D_{ik}^{\tau_{ij}}/2$  are the sum of the turbulent and molecular fluxes of the SGS stress and SGS kinetic energy, respectively. The production of the SGS stress  $P_{ij}$  and the production of SGS kinetic energy  $P = P_{ii}/2$  are known because they can be expressed in terms of  $\tau_{ij}$  and filtered gradients, but the SGS pressure strain  $\Pi_{ij}$  and the SGS dissipation rate tensor  $\epsilon_{ij}$  need to be modelled. These terms read

$$\begin{aligned} P_{ij} = & -\tau_{ik} \frac{\partial \widetilde{u_j}}{\partial x_k} - \tau_{jk} \frac{\partial \widetilde{u_i}}{\partial x_k} \\ = & K_{SGS} \left[ -\frac{4}{3} \widetilde{S}_{ij} - (a_{ik} \widetilde{S}_{kj} + \widetilde{S}_{ik} a_{kj}) + (a_{ik} \widetilde{\Omega}_{kj} - \widetilde{\Omega}_{ik} a_{kj}) \right], \end{aligned} \quad (2.4)$$

$$\Pi_{ij} = \frac{2}{\rho} (\widetilde{S}_{ij} p - \widetilde{S}_{ij} \widetilde{p}), \quad (2.5)$$

$$\epsilon_{ij} = 2\nu \left( \frac{\partial \widetilde{u_i}}{\partial x_k} \frac{\partial u_j}{\partial x_k} - \frac{\partial \widetilde{u_i}}{\partial x_k} \frac{\partial \widetilde{u_j}}{\partial x_k} \right), \quad (2.6)$$

where  $\widetilde{S}_{ij} = (\partial \widetilde{u_i} / \partial x_j + \partial \widetilde{u_j} / \partial x_i) / 2$  is the resolved rate of strain;  $\widetilde{\Omega}_{ij} = (\partial \widetilde{u_i} / \partial x_j - \partial \widetilde{u_j} / \partial x_i) / 2$  is the resolved rotation rate tensor; and  $\widetilde{p}$  is the resolved pressure. The corresponding RANS expressions for  $P_{ij}$ ,  $\Pi_{ij}$  and  $\epsilon_{ij}$  are easily obtained by replacing the filter operator  $\widetilde{\cdot}$  by an ensemble average and by using the Reynolds

decomposition  $u = \tilde{u} + u'$  and the rule  $\widetilde{\tilde{u}u'} = 0$ . The latter rule is not valid in LES, i.e.  $\widetilde{\tilde{u}u'} \neq 0$ . Consequently, by decomposing the velocity as  $u_i = \tilde{u}_i + u'_i$  and the pressure as  $p = \tilde{p} + p'$  the SGS pressure strain can be written as

$$\Pi_{ij} = \frac{2}{\rho} ((\tilde{p}\tilde{S} - \tilde{p}'\tilde{S}') + \widetilde{p'S} + \widetilde{\tilde{p}S'} + \widetilde{p'S'}). \quad (2.7)$$

In contrast to RANS models there are correlation terms of the type  $\widetilde{\tilde{S}_{ij}p'}$  in (2.7). Although the Reynolds axioms are not valid in LES we assume that it is possible to model the terms  $\Pi_{ij}$  and  $\epsilon_{ij}$  using the same modelling approach as in RANS simulations, i.e. in terms of filtered gradients and  $\tau_{ij}$ . We follow the steps of Wallin & Johansson (2000) and use a slightly modified version of the general linear model by Launder, Reece & Rodi (1975) for (2.5) and an isotropic model for the dissipation tensor (2.6). The models read

$$\begin{aligned} \Pi_{ij} = & -\epsilon c_1 a_{ij} + K_{sgs} \left[ \frac{3}{5} \tilde{S}_{ij} + \frac{9c_2 + 6}{11} \left( a_{ik} \tilde{S}_{kj} + \tilde{S}_{ik} a_{kj} - \frac{2}{3} a_{km} S_{mk} \delta_{ij} \right) \right. \\ & \left. + \frac{7c_2 - 10}{11} (a_{ik} \tilde{\Omega}_{kj} - \tilde{\Omega}_{ik} a_{kj}) \right], \end{aligned} \quad (2.8)$$

$$\epsilon_{ij} = \epsilon \frac{2}{3} \delta_{ij}, \quad (2.9)$$

where  $c_1$  is a relaxation coefficient analogous to the Rotta constant;  $c_2$  is a model parameter associated with the rapid part of  $\Pi_{ij}$ , i.e. the part of  $\Pi_{ij}$  that depends directly on changes in the resolved velocity gradients; and  $\epsilon = \epsilon_{ii}/2$ . Model (2.8) for  $\Pi_{ij}$  applied here only differs from the original RANS model by the coefficient in front of  $\tilde{S}_{ij}$ . We choose a slightly reduced coefficient in order to increase the predicted SGS anisotropy. The model for the rapid part of  $\Pi_{ij}$  is assumed to account for all rapid terms in (2.7). Also the term  $\widetilde{p'S}$  is rapid in the sense that it directly responds to changes in the resolved velocity field. The RANS model by Wallin & Johansson (2000) assumes  $c_2 = 5/9$  which is close to the values suggested for RANS simulation. For the present SGS stress model we apply the same value,  $c_2 = 5/9$ , which considerably simplifies the model. Although the model for the rapid part of  $\Pi_{ij}$  is very similar to the RANS version it is a reasonable model for LES. The *a priori* tests in the Appendix shows that the model captures the behaviour of the components reasonably well, and we believe there is no clear reason to construct a more complicated model. The model parameter  $c_1$  is determined in §5.2 using DNS data for the slow part of  $\Pi_{ij}$ .

The derivation of the EARSM (Wallin & Johansson 2000) involves the weak equilibrium assumption implying that the advection and diffusion of the Reynolds stress anisotropy are neglected. This can cause problems in regions with strong inhomogeneity and a low level of turbulence production. Nevertheless, the EARSM has been successfully applied to shear and rotating flows. In LES the left-hand side of (2.2) is of course not negligible in a local sense because the advection of  $a_{ij}$  is a fluctuating property. However, we expect the weak equilibrium assumption to be a reasonable approximation with a coarse filter scale, at least in the mean sense. This assumption allows for an explicit SGS model that can account for rotation in a natural way and a treatment of the subgrid anisotropy. In addition to the weak equilibrium assumption we assume  $P = \epsilon$  which strongly simplifies the model. This assumption cannot be made in RANS models, but in §4 we show that this assumption is quite reasonable on the subgrid level. By applying the weak equilibrium assumption

and  $P = \epsilon$  we obtain from (2.2)

$$0 = P_{ij} - \epsilon_{ij} + \Pi_{ij}. \quad (2.10)$$

Note that this is an equilibrium assumption different from the weak equilibrium assumption applied in the corresponding RANS model. The models for  $\Pi_{ij}$  and  $\epsilon_{ij}$  imply

$$c_1 a_{ij} = \tau^* \left( -\frac{11}{15} \tilde{S}_{ij} + \frac{4}{9} (a_{ik} \Omega_{kj} - \Omega_{ik} a_{kj}) \right), \quad (2.11)$$

where  $\tau^* = K_{SGS}/\epsilon$  is the SGS time scale. We solve (2.11) using the ansatz

$$a_{ij} = \beta_1 \tau^* \tilde{S}_{ij} + \beta_4 \tau^{*2} (\tilde{S}_{ik} \tilde{\Omega}_{kj} - \tilde{\Omega}_{ik} \tilde{S}_{kj}), \quad (2.12)$$

where  $\beta_1$ ,  $\beta_2$  and  $\beta_4$  are functions of  $\tilde{S}_{ij}$  and  $\tilde{\Omega}_{ij}$  and the model parameters. The ansatz is strictly valid only for two-dimensional resolved velocity fields according to the Cayley–Hamilton theorem, but it represents a reasonable approximation for several three-dimensional fields as well (Wallin & Johansson 2000). By solving (2.11) using (2.12) we finally obtain an explicit algebraic model for the SGS stress,

$$\tau_{ij} = K_{SGS} \left( \frac{2}{3} \delta_{ij} + \beta_1 \tau^* \tilde{S}_{ij} + \beta_4 \tau^{*2} (\tilde{S}_{ik} \tilde{\Omega}_{kj} - \tilde{\Omega}_{ik} \tilde{S}_{kj}) \right), \quad (2.13)$$

where  $\beta_1$  and  $\beta_4$  are functions of  $\tilde{\Omega}_{ij}$  and the model parameters as follows:

$$\beta_1 = -\frac{33}{20} \frac{9c_1/4}{[(9c_1/4)^2 - 2II_\Omega]}, \quad \beta_4 = -\frac{33}{20} \frac{1}{[(9c_1/4)^2 - 2II_\Omega]}, \quad (2.14)$$

where  $II_\Omega = \tau^{*2} \tilde{\Omega}_{ik} \tilde{\Omega}_{ki}$ . (Note that  $II_\Omega \leq 0$ .) The unknown quantities that we need to model are the SGS kinetic energy,  $K_{SGS}$ , and the SGS time scale,  $\tau^*$ . We will here derive one dynamic and one non-dynamic model for  $K_{SGS}$  and  $\tau^*$ , respectively.

### 2.1. The SGS kinetic energy: dynamic version

We model the SGS kinetic energy in terms of the squared Smagorinsky velocity scale  $\Delta |\tilde{S}_{ij}|$ :

$$K_{SGS} = c \Delta^2 |\tilde{S}_{ij}|^2. \quad (2.15)$$

Here  $\Delta$  is the filter scale;  $|\tilde{S}_{ij}| = (2\tilde{S}_{ij}\tilde{S}_{ij})^{0.5}$ ; and  $c$  is a dynamic parameter which is determined using Germano's identity,

$$\widehat{\tilde{u}_i \tilde{u}_i} - \hat{\tilde{u}_i} \hat{\tilde{u}_i} = c \hat{\Delta}^2 \widehat{2\tilde{S}_{ij}\tilde{S}_{ij}} - c \Delta^2 \widehat{2\tilde{S}_{ij}\tilde{S}_{ij}}, \quad (2.16)$$

where  $\hat{\cdot}$  denotes an explicit test filter with the filter width  $\hat{\Delta}$ . Note that this equation is not over-determined as is the case of the dynamic Smagorinsky model. Hence, the number of filter operations needed to obtain the dynamic constant is smaller.

In the following we denote  $L = \widehat{\tilde{u}_i \tilde{u}_i} - \hat{\tilde{u}_i} \hat{\tilde{u}_i}$  and  $M = \hat{\Delta}^2 \widehat{2\tilde{S}_{ij}\tilde{S}_{ij}} - \Delta^2 \widehat{2\tilde{S}_{ij}\tilde{S}_{ij}}$ . Equation (2.16) is then given by  $L = cM$ . The dynamic constant can be calculated according to  $c = \langle L \rangle / \langle M \rangle$ , but we have experienced that such determination can become singular near the wall in high-Reynolds-number channel flow. In this paper we have used  $c = \langle LM \rangle / \langle M^2 \rangle$  and clipping to avoid negative values, which is stable and without any backscatter. The test filter function is a two-dimensional spectral cutoff filter.

There is no dynamic determination of  $\epsilon$ . Instead the time scale of the SGS velocity field is estimated by

$$\tau^* = \frac{K_{SGS}}{\epsilon} = c_3 |\tilde{S}_{ij}|^{-1}, \quad (2.17)$$

implying that  $\epsilon$  is approximated with  $\epsilon = c_3^{-1} c \Delta^2 |\tilde{S}_{ij}|^3$ . A constant value of  $c_3$  works well for  $\tau^*$  in high-Reynolds-number isotropic turbulence (see Marstorp, Brethouwer & Johansson 2007), but it is not a good approximation in low-Reynolds-number inhomogeneous flows involving strong mean velocity gradients. As a remedy for this problem the parameter  $c_3$  is modelled in terms of  $\Delta$ ,  $K_{SGS}$  and  $|\tilde{S}_{ij}|$ :

$$c_3 = c'_3 1.5C^{1.5} \frac{\sqrt{K_{SGS}}}{2C_s \Delta |\tilde{S}_{ij}|}, \quad (2.18)$$

where  $c'_3$  is a constant;  $C$  is the Kolmogorov constant; and  $2C_s \Delta |\tilde{S}_{ij}|$  is a Smagorinsky type of velocity scale using a constant  $C_s$ . The factor  $1.5C^{1.5}$  is an estimate of the non-dimensional SGS shear in high-Reynolds-number isotropic turbulence (see Pope 2000), and the ratio  $\sqrt{K_{SGS}}/(2C_s \Delta |\tilde{S}_{ij}|)$  accounts for the deviation from equilibrium because it naturally decreases as the wall is approached. With the dynamic model for  $K_{SGS}$  above the expression reduces to

$$\tau^* = c'_3 \frac{1.5C^{1.5} \sqrt{c}}{2C_s} |\tilde{S}_{ij}|^{-1}. \quad (2.19)$$

By including the dynamic parameter  $c$  in the model for  $c_3$ , the time scale  $\tau^*$  is reduced near the wall and when there is laminarization.

## 2.2. The SGS kinetic energy: non-dynamic version

A non-dynamic version of the new explicit algebraic model is desirable as a complement because any dynamic procedure is computationally expensive and complicated to implement. Moreover, there are situations in which the dynamic procedure is inappropriate, i.e. in complex geometries without any homogeneous directions or in an LES with very coarse resolution in which the test filter scale becomes very large.

The aim is to develop a non-dynamic version of the new model based on a non-dynamic model for the SGS kinetic energy which can deal with laminarization. Our model is based on the approximation  $P = \epsilon$ , and dimensional analysis leads to

$$\frac{K_{SGS}^{3/2}}{\epsilon} = C_k \Delta, \quad (2.20)$$

where  $C_k$  is a constant of order one;  $C_k$  is not a universal constant and is sometimes determined using a dynamic procedure (see for example Ghosal *et al.* 1995). In this paper we will use a constant and scale-independent  $C_k$  in order to obtain an efficient non-dynamic model for  $K_{SGS}$ . To first order, if only the eddy-viscosity part is considered in (2.13), we have

$$P\epsilon = -\tau_{ij} \tilde{S}_{ij} \epsilon = (-\beta_1) K_{SGS}^2 \tilde{S}_{ij} \tilde{S}_{ij}. \quad (2.21)$$

If we now assume that  $P = \epsilon$  we get

$$\epsilon^2 = -\frac{1}{2} \beta_1 K_{SGS}^2 |\tilde{S}_{ij}|^2. \quad (2.22)$$

The approximation  $P = \epsilon$  will later be validated (§4). Finally, by inserting  $\epsilon$  into (2.20) we get

$$K_{SGS} = -\frac{1}{2} \beta_1 C_k^2 \Delta^2 |\tilde{S}_{ij}|^2. \quad (2.23)$$

Although  $\beta_1$  accounts for the influence of system rotation by reducing  $K_{SGS}$  in laminarized regions it does not impose the correct near-wall behaviour for the SGS

kinetic energy. Additional wall damping is thus needed. In the present LES we apply standard van Driest near-wall damping of  $K_{SGS}$ .

The time scale cannot be modelled using the same strategy as for the dynamic case because such a model would result in an implicit expression for  $\beta_1$ . Instead, we use a constant  $c_3$  for the non-dynamic case,

$$\tau^* = c_3 |\tilde{S}_{ij}|^{-1}. \quad (2.24)$$

### 2.3. System rotation

In a rotating frame of reference, the system rotation rate vector  $\Omega_i^s$  enters (2.2) explicitly through two different terms (see Wallin & Johansson 2000). The first term is a consequence of the transformation of the production term,

$$P_{ij} = K_{SGS} \left[ -\frac{4}{3} \tilde{S}_{ij} - (a_{ik} \tilde{S}_{kj} + \tilde{S}_{ik} a_{kj}) + (a_{ik} (\tilde{\Omega}_{kj} + \Omega_{kj}^s) - (\tilde{\Omega}_{ik} + \Omega_{ik}^s) a_{kj}) \right], \quad (2.25)$$

where  $\Omega_{ij}^s = \epsilon_{jik} \Omega_k^s$  is the system rotation tensor. Note that the production term also appears in the model for  $\Pi_{ij} - \epsilon_{ij}$ . The second term arises from the transformation of the advection term,

$$C_{ij}^{adv} = K_{SGS} (a_{ik} \Omega_{kj}^s - \Omega_{ik}^s a_{kj}). \quad (2.26)$$

With  $c_2 = 5/9$  the transformed production and advection terms can be accounted for by modifying  $\tilde{\Omega}_{ij}$  into the ‘effective’ rotation rate tensor according to

$$\tilde{\Omega}_{ij}^R = \tilde{\Omega}_{ij} + 13/4 \epsilon_{ikj} \Omega_k^s. \quad (2.27)$$

This is a formal modification that is important to include in order to extend the model to rotating flows. The system rotation modifies both the amplitude of the model coefficients  $\beta_1$  and  $\beta_4$  and the anisotropy of the SGS stress through the term  $(\tilde{S}_{ik} \tilde{\Omega}_{kj}^R - \tilde{\Omega}_{ik}^R \tilde{S}_{kj})$ . The factor 13/4 is obtained as a direct consequence of adding the contributions, associated with system rotation, from the production, the pressure/strain rate model and the advection of the frame-invariant part of the SGS stress anisotropy, in (2.10).

The contribution from the advection term is a result of the approximation that the weak equilibrium assumption is valid in the rotating frame only. This is a good approximation for RANS models, and it corresponds to the assumption that the flow is statistically homogeneous in the rotating frame only (see Gatski & Wallin 2004). If the contribution from the advection is neglected, i.e. if the weak equilibrium assumption is assumed to be valid in the fixed inertial frame of reference only, we have  $\tilde{\Omega}_{ij}^R = \tilde{\Omega}_{ij} + \epsilon_{ikj} \Omega_k$  instead of  $\tilde{\Omega}_{ij}^R = \tilde{\Omega}_{ij} + 13/4 \epsilon_{ikj} \Omega_k$ . However, we believe that the latter case,  $\tilde{\Omega}_{ij}^R = \tilde{\Omega}_{ij} + 13/4 \epsilon_{ikj} \Omega_k$ , is more accurate because the flow is only approximately homogeneous in the rotating frame. It should be noted that the rotation contribution discussed here is obtained when the advective derivative operates on the frame-invariant part of the SGS stress anisotropy tensor only. The contributions from the frame-dependent parts are not incorporated here. This simplification provides a way of having the same model form as for the RANS case.

Speziale (1985) investigated the transformation properties of the SGS stress tensor and found that the SGS force  $\partial \tau_{ij} / \partial x_j$  is frame invariant with respect to system rotation whereas  $\tau_{ij}$  is not. Therefore, he claimed that SGS stress models should satisfy the frame invariance of the SGS force. If taken into account, this criterion implies that the modelling approach proposed here is not fully appropriate. More specifically, in the present case the use of the term proportional to  $S_{ik} \Omega_{kj} - \Omega_{ik} S_{kj}$  leads to a frame

dependence of the divergence of the SGS stress. In order to address this issue to some extent, computations of rotating and non-rotating channel flow have been performed using an SGS stress model that has been extended with the term  $\beta_4 K_{SGS} \tau^{*2} (\Omega_{ik} \Omega_{kj} - 1/3 \Omega_{mn} \Omega_{nm} \delta_{ij})$ . The corresponding model with constant  $\beta_4$  would fulfil the above criterium. For the model proposed here,  $\beta_4$  has a spatial dependence, and hence the criterium is fulfilled only to zeroth order. We still feel that the extended model can be mentioned shortly here for comparative purposes. Computations indicate that the extension gives no prediction improvements for rotating channel flow and that it negatively affects the predictions for the non-rotating case. For instance the centreline velocity deviates by 10–15 % compared to the original model and DNS. The extended model will not be subject of further discussion, since this would not contribute to the present paper.

The divergence invariance criterion of Speziale (1985) has been questioned by other authors, and nonlinear frame-dependent SGS stress models have been proposed. Kosović (1997) includes the tensor  $S_{ik} \Omega_{kj} - \Omega_{ik} S_{kj}$  without including any extra ‘corrective’ terms and argues that this is correct. He also reports on ‘a significant improvement’. Furthermore, it is easy to see that the frame invariance criterion is as applicable to the Reynolds stresses in RANS simulation as it is to the SGS stresses in LES. On the other hand, it is possible to formulate an EARSM that is an exact solution to the underlying transport equation, for some types of rotating flows (e.g. rotating homogeneous flow), but does not fulfil the divergence criterion (see for instance Wallin & Johansson 2000; Gatski & Wallin 2004). This illustrates that the frame invariance principle of Speziale (1985) is not always compatible with the physics of the transport equation for the stress anisotropy.

In accordance with Speziale (1985) we assume that the filter function does not depend on the frame of reference. Speziale (1985) showed that this is true only if the filter function satisfies  $G(\mathbf{x}) = G(|\mathbf{x}|)$ . This requirement is satisfied by for example the isotropic Gaussian filter and the spherical top-hat filter, but it is not satisfied by for example the spectral cutoff filter. A filter function that does not commute with the temporal and spatial differential operators introduces a commutation error. This was studied by Fureby & Tabor (1997) who concluded that the commutation error for turbulent channel flow at  $Re_\tau = 180$  was small, in general less than 3 %. For the purpose of the present study, the assessment of the commutation error is out of scope. However, with the study of Fureby & Tabor (1997) in mind, we find it reasonable to believe that the commutation error should have a small effect on the predictions compared to the effects of using different SGS stress models.

### 3. Simulations

LESs of spanwise rotating turbulent channel flow at wall friction Reynolds number  $Re_\tau = 180$  and a resolution of  $32 \times 33 \times 32$  are performed in a box with the dimensions  $4\pi\delta \times 2\delta \times 2\pi\delta$  in the streamwise, wall-normal and spanwise direction respectively. The code uses spectral representation in the streamwise ( $x$ ) and spanwise ( $z$ ) directions and uses a Chebyshev representation in the wall-normal ( $y$ ) direction (see Chevalier *et al.* 2007). The grid spacings in wall units are  $\Delta x^+ = 71$ ,  $\Delta z^+ = 36$  and on average  $\langle \Delta y^+ \rangle = 11$ . The LES results for the rotating cases are compared to the DNS data of Grundestam *et al.* (2008). Their DNS data are represented on  $192 \times 129 \times 160$  grid points and are filtered to  $32 \times 32$  using a spectral cutoff filter in the homogeneous directions. We have also employed a sharp cutoff filter in Chebyshev space as an explicit filter in the normal direction, but it is omitted here, since it only had a very



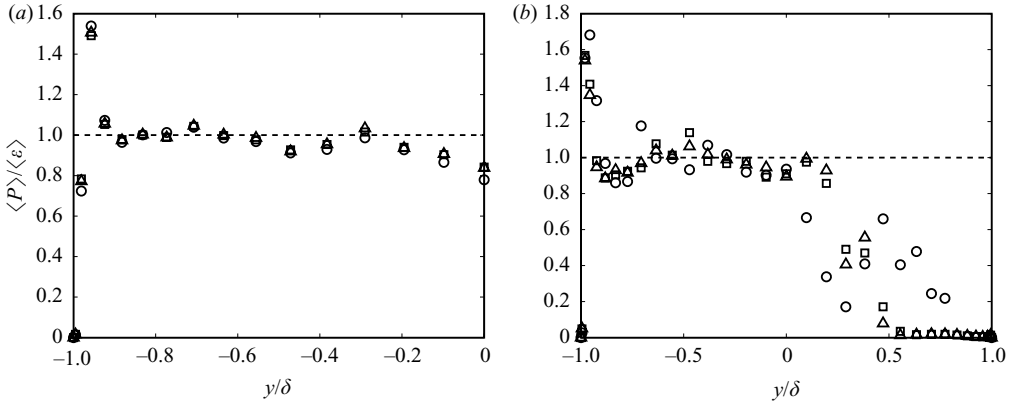


FIGURE 1. The ratio  $\langle P \rangle / \langle \epsilon \rangle$  according to filtered DNS at various filter scales: (a)  $Ro^+ = 0$  and (b)  $Ro^+ = 37$ . The symbols are as follows:  $\circ$ ,  $\sqrt{\Delta_x \Delta_z^+} = 50$ ;  $\square$ ,  $\sqrt{\Delta_x \Delta_z^+} = 25$ ;  $\triangle$ ,  $\sqrt{\Delta_x \Delta_z^+} = 17$ .

small impact on the filtered DNS data. Because of the explicit filtering the filtered DNS data are not incompressible. For the turbulence intensities we compare LES and DNS by adding the mean SGS stresses to the mean resolved stresses. This can be done with the new model because a model for the SGS kinetic energy is used, but it cannot be done with traceless models such as the Smagorinsky model (see Winckelmans, Jeanmart & Carati 2002). For that reason we supply the Smagorinsky model results with the trace  $2K_{SGS}$  computed from DNS when we compare the intensities. The channel is rotating about the spanwise axis, and the influence of system rotation can be measured by the rotation number defined as  $Ro^+ = 2\Omega^s \delta / u_\tau$ . In rotating channel flow the wall friction velocity is defined as

$$u_\tau = \sqrt{\frac{1}{2}(u_\tau^s)^2 + \frac{1}{2}(u_\tau^u)^2}, \quad (3.1)$$

where the  $u_\tau^s$  and  $u_\tau^u$  are the wall friction velocities at the stable and unstable sides of the channel respectively. Rotation numbers ( $Ro^+$ ) from 0 to 110 are considered. For the non-rotating case we carry out a comparison with the DNS by Schlatter, Stolz & Kleiser (2004). In addition to LES of spanwise rotation, LES of streamwise rotating channel flow is performed at  $Ro^+ = 10$  using the resolution  $48 \times 49 \times 48$  and the same computational box and Reynolds number as in the previous case. The LES results were compared to the DNS data by Oberlack *et al.* (2006).

Finally, LESs of non-rotating channel flow at  $Re_\tau = 950$  are performed using three different resolutions:  $(64 \times 96 \times 64)$ ,  $(96 \times 96 \times 96)$  and  $(128 \times 128 \times 128)$ . Also LESs of spanwise rotating channel flow at  $Re_\tau = 950$  are performed using the resolution  $(128 \times 128 \times 128)$ . In every case, the LESs are performed in a box with the dimensions  $4\pi\delta \times 2\delta \times 2\pi\delta$  in the streamwise, wall-normal and spanwise direction respectively.

#### 4. Validation of the approximation $P = \epsilon$ and the equilibrium assumption $0 = P_{ij} + \Pi_{ij} - \epsilon_{ij}$

We have applied the approximation  $P = \epsilon$  to derive the new models. To validate this assumption we have calculated  $\langle P \rangle / \langle \epsilon \rangle$  with and without rotation. From figure 1 we see that for the non-rotating case  $\langle P \rangle = \langle \epsilon \rangle$  is a good approximation away from

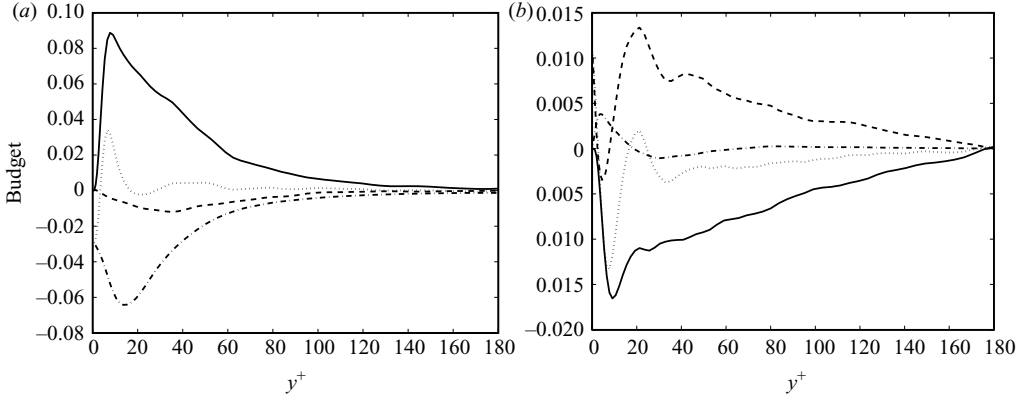


FIGURE 2. The budget terms (a)  $\langle P_{11} \rangle$ ,  $\langle \Pi_{11} \rangle$  and  $\langle \epsilon_{11} \rangle$ , and (b)  $\langle P_{12} \rangle$ ,  $\langle \Pi_{12} \rangle$  and  $\langle \epsilon_{12} \rangle$  with filter width  $\sqrt{\Delta_x \Delta_z^+} = 25$ . Production is denoted by the solid line, pressure strain correlation by the dashed line, dissipation by the dash-dotted line and sum by the dotted line.

the solid walls for a wide range of filter scales. For the rotating case it is not a good approximation close to the wall (where stabilization occurs) at the stabilized side of the channel. Even though the approximation  $P = \epsilon$  is poor near the wall, we will later show that the model which uses this approximation gives fairly good *a posteriori* predictions.

The approximation  $P = \epsilon$  and the weak equilibrium assumption result in (2.10) which considerably simplifies the SGS model compared to the corresponding RANS model. Again, we validate this assumption by computing the averaged components from filtered DNS of turbulent channel flow, i.e.

$$0 = \langle P_{ij} \rangle + \langle \Pi_{ij} \rangle - \langle \epsilon_{ij} \rangle. \quad (4.1)$$

Figure 2(a) shows the diagonal streamwise component of (4.1) at the resolution  $\Delta_x^+ = 47$  and  $\Delta_z^+ = 24$  which is typical for LES. We can see that the dissipation nearly cancels the production, whereas the pressure strain term is small. The sum of the terms is very close to zero except near the wall. The same results apply to the other diagonal components (results not shown here). The off-diagonal component of (4.1) is shown in figure 2(b). Here, the pressure strain nearly balances the production term, whereas the dissipation term is small. Again, the sum of the three terms is small except near the wall. Thus, the equilibrium assumption  $0 = P_{ij} + \Pi_{ij} - \epsilon_{ij}$  seems to be justified for LES except very near the solid walls. However, even though the equilibrium assumption is not valid near the wall, the dynamic model for the SGS kinetic energy and the model for  $c_1$  impose a correct near-wall behaviour of the eddy viscosity (see § 5.2).

## 5. Determination of the model parameters

In this section we validate the models for  $K_{SGS}$  and  $\tau^*$  and determine the model constants  $C_k$  and  $c'_3$  using LESs and *a priori* results. We also evaluate the model parameter  $c_1$  *a priori* and propose a model for  $c_1$ .

### 5.1. The SGS kinetic energy and time scale

Figure 3 shows the modelled mean SGS kinetic energy compared to the SGS kinetic energy computed from DNS for  $Ro^+ = 0$  and 37. For  $Ro^+ = 0$ , both the non-dynamic

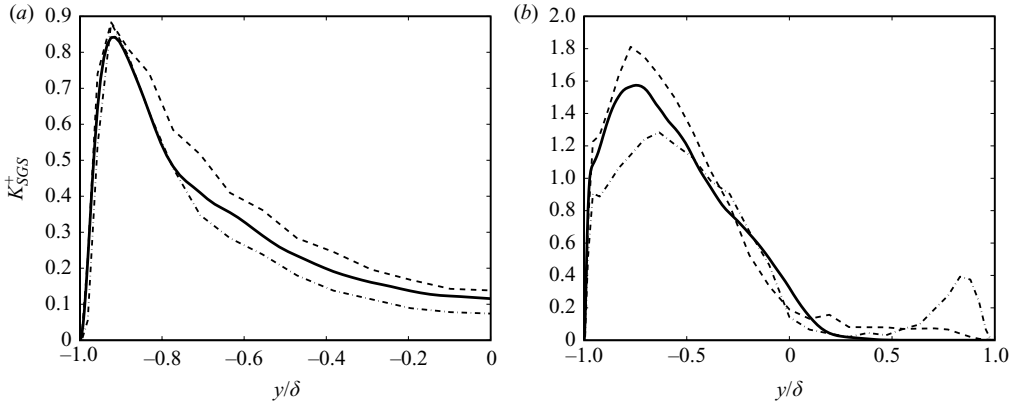


FIGURE 3. The mean SGS kinetic energy: (a)  $Ro^+ = 0$  and (b)  $Ro^+ = 37$ . The dynamic model is represented by the dashed line, the non-dynamic model by the dash-dotted line and DNS by the solid line.

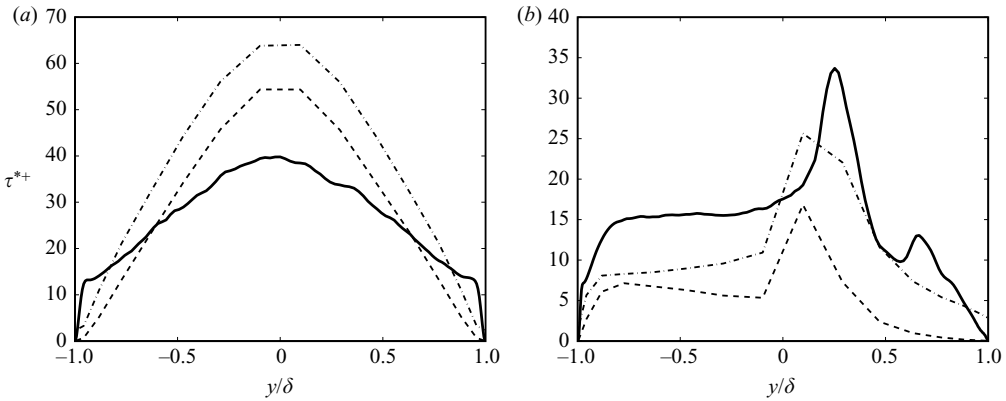


FIGURE 4. The SGS time scale  $\tau^{*+}$  in terms of wall units: (a)  $Ro^+ = 0$  and (b)  $Ro^+ = 37$ . The dynamic model is denoted by the dashed line, the non-dynamic model by the dash-dotted line and DNS by the solid line.

model (2.23) with  $C_k = 0.4$  and the dynamic model (2.15) for  $K_{SGS}$  capture the behaviour of  $\langle K_{SGS} \rangle$  fairly well. For  $Ro^+ = 37$ , the non-dynamic model is able to capture the behaviour of  $\langle K_{SGS} \rangle$  including the laminarization at the stabilized side of the channel ( $y/\delta \approx 0.3$ ). However,  $\langle K_{SGS} \rangle$  is overpredicted close to the wall at the stabilized side of the channel because of the excessive contribution from the mean velocity gradient in that region. The dynamic model for  $K_{SGS}$  performs better in that respect and captures the behaviour of  $\langle K_{SGS} \rangle$  at the stabilized side of the channel more accurately. Thus, the non-dynamic model for  $K_{SGS}$  represents a computationally efficient model that can capture the laminarization to some extent, whereas the dynamic model for  $K_{SGS}$  is the most accurate.

Figure 4 shows the performance of the dynamic model (2.19) for  $\tau^*$  using  $c'_3 = 2.5$  and  $C_s = 0.10$  and the performance of the non-dynamic model (2.24) using  $c_3 = 2.2$ . Both models capture the behaviour of the SGS time scale fairly well, but they overpredict  $\tau^*$  at  $Ro^+ = 0$  and underpredict  $\tau^*$  at  $Ro^+ = 37$ . The dynamic model is the most accurate because it naturally reduces  $\langle \tau^* \rangle$  to zero as the wall is approached.

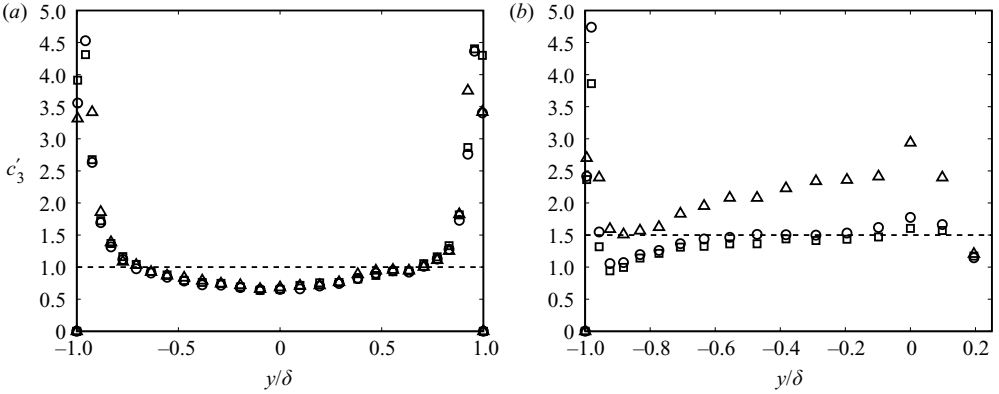


FIGURE 5. The model parameter  $c'_3$  from DNS at different filter scales: (a)  $Ro^+ = 0$  and (b)  $Ro^+ = 37$ . The symbols are as in figure 1.

The model parameter  $c'_3$  is evaluated *a priori* in figure 5 using  $C_s = 0.10$ . The results show that  $c'_3$  is fairly independent of filter scale. The value  $c'_3 \approx 1-2$  suggested by the *a priori* test is slightly lower than the value  $c'_3 \approx 2.5$  applied in the LES we carry out later.

### 5.2. A priori test of $c_1$

Assuming that the filter operator commutes with the differential operator the Poisson equation for the subgrid pressure reads

$$\frac{1}{\rho} \frac{\partial^2 p'}{\partial x_i \partial x_i} = - \frac{\partial^2}{\partial x_i \partial x_j} [(\tilde{u}_i \tilde{u}_j - \widetilde{u_i u_j}) + (\tilde{u}_i u'_j - \widetilde{u_i u'_j}) + (u'_i \tilde{u}_j - \widetilde{u'_i \tilde{u}_j}) + (u'_i u'_j - \widetilde{u'_i u'_j})]. \quad (5.1)$$

Similar to the RANS case the subgrid pressure  $p'$  involves a rapid part that depends on the filtered (resolved) gradients and a slow part that only depends on the subgrid velocity field, i.e.  $p' = p'_{rapid} + p'_{slow}$ , where

$$\frac{1}{\rho} \frac{\partial^2 p'_{slow}}{\partial x_i \partial x_i} = - \frac{\partial}{\partial x_i} \left( \frac{\partial (u'_i u'_j - \widetilde{u'_i u'_j})}{\partial x_j} \right). \quad (5.2)$$

If we solve the Poisson equation for  $p'_{slow}$  we can compute the slow part of the subgrid pressure strain,

$$\Pi_{ij}^{slow} = p'_{slow} \widetilde{S'_{ij}}. \quad (5.3)$$

The other terms in (2.7) depend on resolved gradients. We determine  $c_1$  by applying the Rotta model  $\Pi_{ij}^{slow} = c_1 \epsilon a_{ij}$ . Since most of the components of  $\Pi_{ij}^{slow}$  have zero mean value, we compute  $c_1$  *a priori* by requiring  $|\Pi_{ij}^{slow}| = c_1 \epsilon |a_{ij}|$ . Using averaging in homogeneous directions we get

$$c_1 = \frac{\langle |\Pi_{ij}^{slow}| K_{SGS} \rangle}{\langle \epsilon |\tau_{kl} - \frac{2}{3} K_{SGS} \delta_{kl}| \rangle}. \quad (5.4)$$

In RANS models the Rotta constant  $c_1^{RANS}$  is a parameter that describes the relaxation rate of the Reynolds stresses towards isotropy. Sjögren & Johansson (2000) showed that  $c_1^{RANS}$  decreases with the turbulence Reynolds number. In wall-bounded flow the local turbulence Reynolds number decreases close to the wall. Therefore, a near-wall

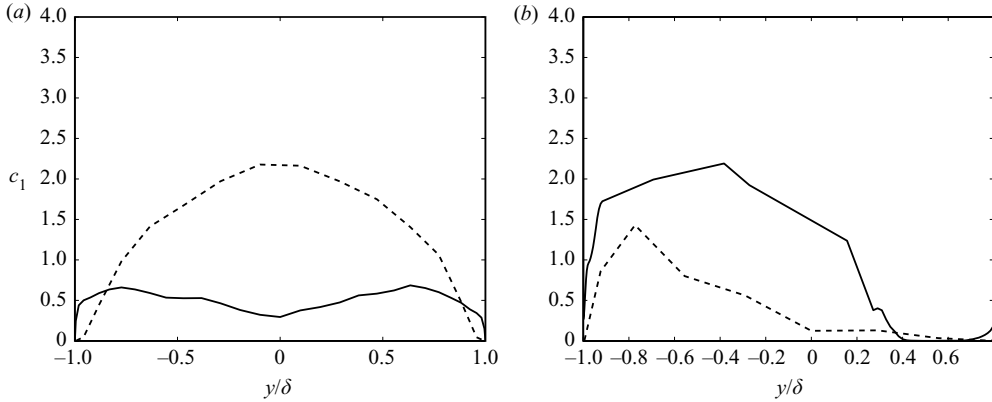


FIGURE 6. *A priori* test of  $c_1$  compared to LES results using the proposed model for  $c_1$  defined in (5.5): (a)  $Ro^+ = 0$  and (b)  $Ro^+ = 37$ . The dynamic model is denoted by the dashed line and DNS by the solid line.

damping of  $c_1^{RANS}$  can be justified, which implies that the return to isotropy becomes weaker when the wall is approached. In LES we expect a similar behaviour for  $c_1$ .

We see from figure 6 that  $c_1$  is a parameter of order one that depends on the local flow properties. It becomes smaller when the wall is approached, but it does not approach zero at the wall. It is also smaller at the stabilized side of the channel where the flow laminarizes.

To model this behaviour the parameter  $c_1$  is described in terms of  $K_{SGS}$ ,  $\tau^*$ ,  $\Delta$  and  $|\tilde{S}_{ij}|$ :

$$c_1 = c'_1 \left( \frac{K_{SGS} |\tilde{S}_{ij}|}{1.5C^{1.5}\epsilon} \right)^{\alpha_1} \left( \frac{K_{SGS}}{4C_s^2 \Delta^2 |\tilde{S}_{ij}|^2} \right)^{\alpha_2}, \tag{5.5}$$

where  $C$  is the Kolmogorov constant;  $\alpha_1$  and  $\alpha_2$  are exponents to be determined from *a priori* tests; and  $c'_1$  is supposed to be a scale independent constant of order one. The factor  $1.5C^{1.5}$  is an estimate of the non-dimensional SGS shear in high-Reynolds-number isotropic turbulence (Pope 2000), and  $4C_s^2 \Delta^2 |\tilde{S}_{ij}|^2$  is an estimate of the SGS kinetic energy using the Smagorinsky velocity scale with constant  $C_s$ . Thus, model (5.5) can account for the deviation from local equilibrium. The *a priori* test in figure 7 using  $\alpha_1 = 0.5$ ,  $\alpha_2 = 1$  and  $C_s = 0.10$  shows that  $c'_1$  is fairly independent of filter scale and attains a value of about  $c'_1 = 2$  in the core region of the non-rotating channel. The *a priori* test suggests a higher and more scale-dependent value  $c'_1 \approx 6$  for the rotating case. If we apply the present dynamic models for  $K_{SGS}$  and  $K_{SGS}/\epsilon$  to (5.5) and use  $\alpha_1 = 0.5$   $\alpha_2 = 1$  we obtain

$$c_1 = c'_1 \sqrt{c'_3} \frac{c^{1.25}}{(2C_s)^{2.5}}. \tag{5.6}$$

As a result,  $c_1$  will be scale invariant in high-Reynolds-number isotropic turbulence and depending on the local flow properties in a case like rotating channel flow. Because  $c_1 \sim c^{1.25}$  the eddy viscosity shows the desired  $y^{+3}$  near-wall scaling in non-rotating channel flow (figure 8). In the present LES we use  $c'_1 = 4.2$  because it was found to give a good *a posteriori* prediction of the SGS anisotropy.

A non-dynamic model for  $c_1$  can be constructed using the same approach as above using the non-dynamic model (2.23) for  $K_{SGS}$ . From the dynamic model for  $c_1$  we see that  $c_1$  is nearly proportional to the dynamic coefficient  $c$ . Here, we simplify (5.5)

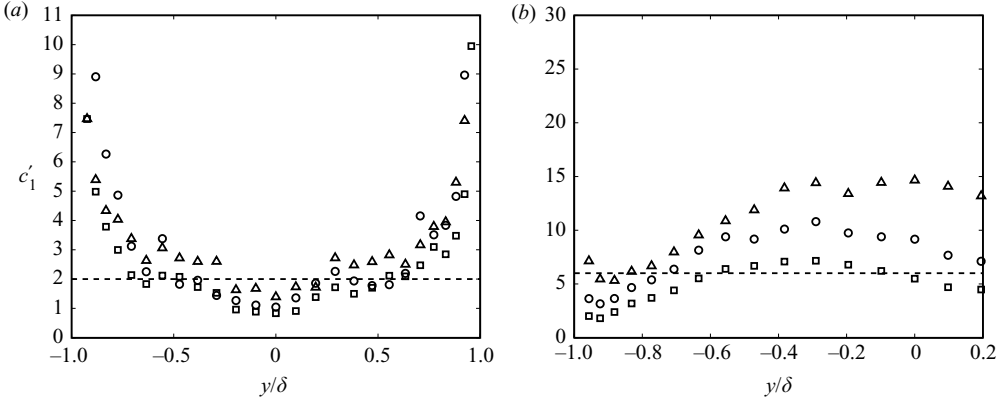


FIGURE 7. *A priori* test of  $c'_1$  at various filter scales: (a)  $Ro^+ = 0$  and (b)  $Ro^+ = 37$ . The symbols are as follows:  $\circ$ ,  $\sqrt{\Delta_x \Delta_z} = 33$ ;  $\square$ ,  $\sqrt{\Delta_x \Delta_z} = 25$ ;  $\triangle$ ,  $\sqrt{\Delta_x \Delta_z} = 17$ .

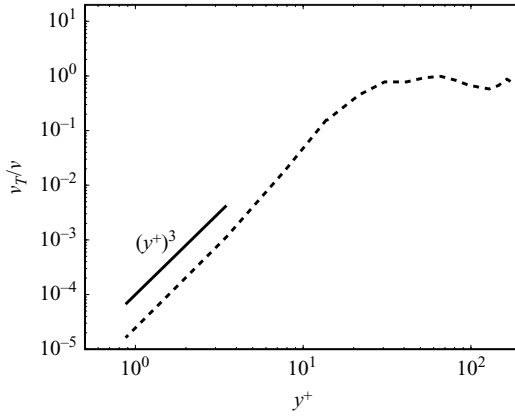


FIGURE 8. Near-wall scaling of the eddy viscosity,  $v_T$ , with the new explicit dynamic model.

by applying  $\alpha_1 = 0$  and  $\alpha_2 = 1$ . As a result  $c_1$  becomes proportional to the dynamic coefficient  $c$ :

$$c_1 = c'_1 \frac{c}{(2C_s)^2}. \tag{5.7}$$

By comparing the dynamic and non-dynamic models for the SGS kinetic energy, i.e. by requiring  $c \Delta^2 |\tilde{S}_{ij}|^2 = -0.5 \beta_1 C_k^2 \Delta^2 |\tilde{S}_{ij}|^2$ , we can express  $c$  in terms of  $\beta_1$  and  $C_k$ :

$$c = -\frac{C_k^2}{2} \beta_1. \tag{5.8}$$

By combining (2.13), (5.7) and (5.8) we obtain an equation for  $c_1$ :

$$c_1 = c'_1 \frac{C_k^2}{(2C_s)^2} \frac{33}{40} \frac{c_1}{(c_1^2 - 2II_\Omega)}. \tag{5.9}$$

The normalization of  $II_\Omega$  is done by the SGS time scale, which depends on  $c$  and is thus proportional to  $c_1$ . By rearranging and using (2.19) and (5.7) we get

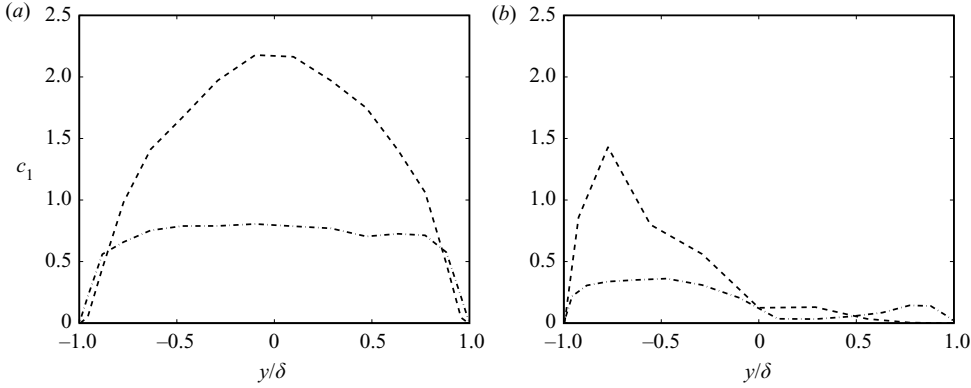


FIGURE 9. Computed  $c_1$ : (a)  $Ro^+ = 0$  and (b)  $Ro^+ = 37$ . The non-dynamic model is denoted by the dash-dotted line and the dynamic model by the dashed line.

$II_\Omega = c_1(c'_3 1.5C^{1.5})^2 (II_\Omega) / (2c'_1 II_S)$ . It is now possible to solve (5.9):

$$c_1 = -\frac{II_\Omega}{2 II_S} \frac{(c'_3 1.5C^{1.5})^2}{c'_1} + \sqrt{\left(\frac{II_\Omega}{2 II_S} \frac{(c'_3 1.5C^{1.5})^2}{c'_1}\right)^2 + c'_1 \frac{33}{40} \frac{C_k^2}{(2C_s)^2}}. \quad (5.10)$$

Figure 9 shows the predicted  $c_1$  using  $c'_1 = 0.6$  and  $c'_3 = 0.4$ . Standard van Driest near-wall damping  $(1 - \exp(-(y^+/15)^2))$  is applied because  $II_\Omega/II_S$  approaches a finite value at the wall. Similar to the dynamic model for  $c_1$  the non-dynamic model (5.10) predicts an approximately constant value in the core region of the non-rotating channel and a reduced  $c_1$  at the stabilized side of the rotating channel.

## 6. Validation of the explicit algebraic SGS stress models in rotating channel flow at $Re_\tau = 180$

LESs of spanwise rotating channel flow are performed using six different SGS models. Four of these models are versions of the new explicit model

$$\tau_{ij} = K_{SGS} \left( \frac{2}{3} \delta_{ij} + \beta_1 \tau^* \tilde{S}_{ij} + \beta_4 \tau^{*2} (\tilde{S}_{ik} \tilde{\Omega}_{kj} - \tilde{\Omega}_{ik} \tilde{S}_{kj}) \right), \quad (6.1)$$

where

$$\beta_1 = -\frac{33}{20} \frac{9c_1/4}{[(9c_1/4)^2 - 2II_\Omega]}, \quad \beta_4 = -\frac{33}{20} \frac{1}{[(9c_1/4)^2 - 2II_\Omega]}. \quad (6.2)$$

The explicit model using (6.1) and the dynamic determination (2.15) of  $K_{SGS}$

$$K_{SGS} = c\Delta^2 |\tilde{S}_{ij}|^2$$

is called hereafter model D. The SGS time scale is modelled using (2.19) with  $c'_3 = 2.4$  and  $C_s = 0.1$ , and the model parameter  $c_1$  is modelled using (5.7) with  $c'_1 = 4.2$  and  $C_s = 0.1$ . The explicit model using (6.1) and the non-dynamic determination (2.23) of  $K_{SGS}$ :

$$K_{SGS} = -\frac{1}{2} \beta_1 C_k^2 \Delta^2 |\tilde{S}_{ij}|^2,$$

where  $C_k = 0.4$ , is called hereafter model ND. The SGS time scale is computed using (2.24) with  $c_3 = 2.2$ , and the model parameter  $c_1$  is modelled using the non-dynamic

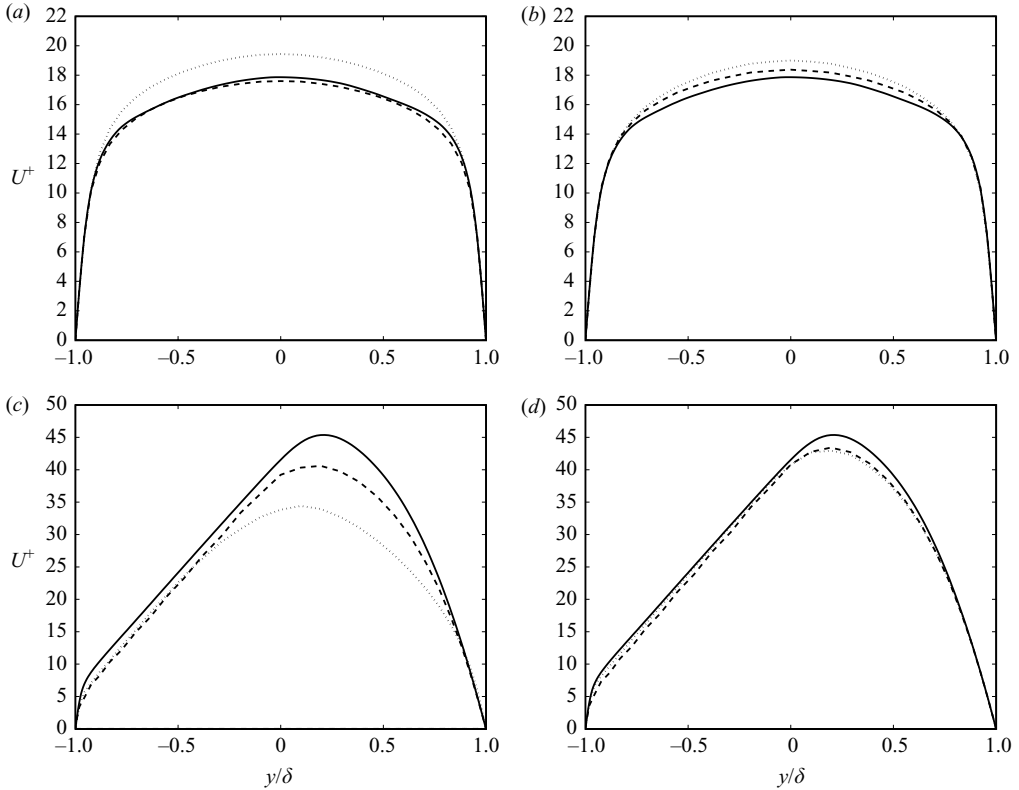


FIGURE 10. Mean velocity profile. (a) Non-dynamic models at  $Ro^+ = 0$ . (b) Dynamic models at  $Ro^+ = 0$ . (c) Non-dynamic models at  $Ro^+ = 37$ . (d) Dynamic models at  $Ro^+ = 37$ . DNS is denoted by the solid line, models D and ND by the dashed line and models DS and S by the dotted line.

model (5.10) with  $C_k = 0.4$ ,  $c'_1 = 0.6$  and  $c'_3 = 0.4$ . In addition, we apply two models which are the same as models D and ND respectively, except that the second constituent term including  $\beta_4$  in (6.1) is neglected. Therefore, these two models only take into account the eddy-viscosity part and are called hereafter model  $D_{EV}$  and model  $ND_{EV}$ , respectively. Model S is the standard Smagorinsky model with van Driest wall damping of the model constant  $C_s^2 = 0.10^2(1 - \exp(-y^+/25))^2$ . Model DS is the dynamic Smagorinsky model with spectral cutoff test filter and averaging of  $C_s$  in the homogeneous directions.

### 6.1. Mean velocity

Figure 10 shows the mean velocity profile for  $Ro^+ = 0$  and 37. Model ND offers significant improvements over model S with wall damping of  $C_s$ . At  $Ro^+ = 0$ , model S overpredicts the mean velocity, whereas model ND does not. In the rotating channel the mean velocity profile has an extended linear range with a slope close to twice the system rotation. The mean velocity is much larger than in the non-rotating case due to the strong damping of the turbulence at the stabilized side of the channel at this high rotation rate as will be shown later. The mean velocity profile is very well predicted by both model DS and model D because the dynamic procedure reduces the SGS dissipation when laminarization occurs. Model S, however, severely underpredicts the mean velocity due to excessive SGS energy dissipation at the stabilized side of the channel. Model ND is better at predicting the reduced SGS dissipation at the



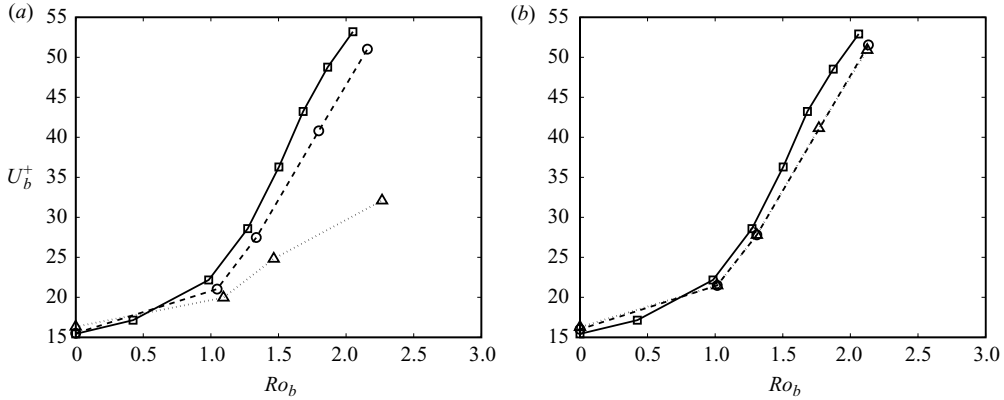


FIGURE 11. Mean bulk velocity at various rotation numbers. (a) Non-dynamic models. (b) Dynamic models. DNS is denoted by the solid line, models D and ND by the dashed line and models DS and S by the dotted line.

stabilized side of the channel, which improves the mean velocity profile. This is due to the explicit dependence on the system rotation included in  $\beta_1$ , which dampens the SGS dissipation at the stabilized side of the channel.

Figure 11 shows the mean bulk velocity defined as

$$U_b^+ = \frac{1}{2\delta u_\tau} \int_{-\delta}^{\delta} \langle u \rangle dy, \quad (6.3)$$

which depends strongly on the rotation number. According to the DNS by Grundestam *et al.* (2008) the mean bulk velocity increases with rotation due to the damping of the turbulence at the stabilized side of the channel. At high  $Ro_b = 2\Omega_s \delta / U_b$  the bulk velocity approaches the laminar value, since the turbulence is also suppressed at the other side of the channel. Because of the included mean gradients a standard eddy-viscosity model predicts a non-zero eddy viscosity even if the flow is laminar. Therefore, model S cannot handle the laminarization and strongly underpredicts  $U_b^+$ . Model ND performs much better in that respect because it can predict the laminarization at the destabilized side of the channel to some extent. Especially, at high rotation rates model ND benefits from the asymptotic behaviour  $\beta_1, \beta_4 \rightarrow 0$  as  $Ro^+ \rightarrow \infty$ . The differences between model DS and model D are small, and both predict the increase of  $U_b^+$  with  $Ro_b$  rather well.

### 6.2. Resolved turbulent kinetic energy and Reynolds stresses

Figure 12 shows the resolved kinetic energy at  $Ro^+ = 0$  and 37. There are no major differences between the model predictions for the non-rotating case. All models capture the location as well as the magnitude of the near-wall peak in  $K$ . This is not the case at  $Ro^+ = 37$  at which there is a very strong damping of the turbulence at the stabilized side of the channel. The DNS data in figure 12 show that the near-wall peak in  $K$  at  $Ro^+ = 37$  at the destabilized side of the channel moves further away from the wall to  $y/\delta \approx -0.65$ . Model S with wall damping of  $C_s$  does not correctly capture this behaviour (see figure 12). The model predicts a near-wall peak in  $K$  and strongly underpredicts  $K$  at both sides of the channel. Model ND gives a better description of the fluctuations;  $K$  peaks at the correct position and the magnitude of  $K$  is in better agreement with DNS. However, model ND overpredicts  $K$  near the wall at the destabilized side of the channel. This is due to the overpredicted SGS

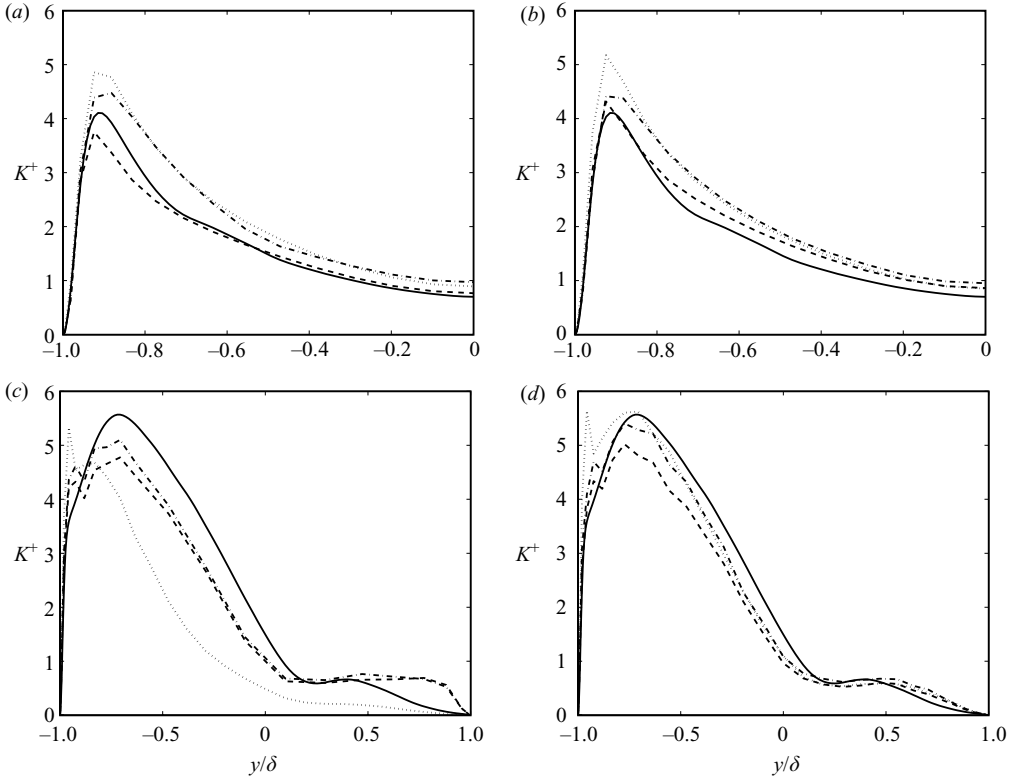


FIGURE 12. Turbulent kinetic energy. (a) Non-dynamic models at  $Ro^+ = 0$ . (b) Dynamic models at  $Ro^+ = 0$ . (c) Non-dynamic models at  $Ro^+ = 37$ . (d) Dynamic models at  $Ro^+ = 37$ . DNS is denoted by the solid line, models DS and S by the dotted line, models D and ND by the dashed line and models  $D_{EV}$  and  $ND_{EV}$  by the dash-dotted line.

kinetic energy close to the wall (see figure 3). Model DS performs better than model S but still predicts a spurious near-wall peak in  $K$ . Model D remedies the problem and predicts a peak in  $K$  at the right position.

Models  $D_{EV}$  and  $ND_{EV}$  perform as well as models D and ND do, respectively, when it comes to the kinetic energy. Hence, the nonlinear term  $\tilde{S}_{ik}\tilde{\Omega}_{kj} - \tilde{\Omega}_{ik}\tilde{S}_{kj}$  appears to have only a very small impact on  $K$ . However, it has an impact on the drain of the resolved enstrophy. This can clearly be seen in the intensity of the streamwise vorticity component,  $\langle\omega_x\rangle^2$ , shown in figure 13. By comparing models D and  $D_{EV}$  we observe that the nonlinear term significantly increases  $\langle\omega_x\rangle^2$  near the wall where the coefficient  $\beta_4$  is large in model D.

Figure 14 shows the Reynolds stresses at  $Ro^+ = 37$  according to models DS, D and  $D_{EV}$ . The system rotation enters explicitly the governing equations and enhances the spanwise and wall-normal fluctuations and reduces the streamwise fluctuations at the destabilized side of the channel in DNS. At  $Ro^+ = 37$ ,  $\langle u'u' \rangle$  is the smallest among the normal stresses, in contrast to the non-rotating case in which  $\langle u'u' \rangle$  is the dominant stress. Model DS overpredicts the near-wall peak in  $\langle u'u' \rangle$  and  $\langle w'w' \rangle$  resulting in a spurious near-wall peak in the turbulence kinetic energy (figure 12d). Also in the region with an approximately constant mean shear,  $-0.6 < y < 0$ , model DS overpredicts the streamwise fluctuations resulting in a too isotropic Reynolds stress tensor. Such underprediction of the anisotropy is also obtained with model

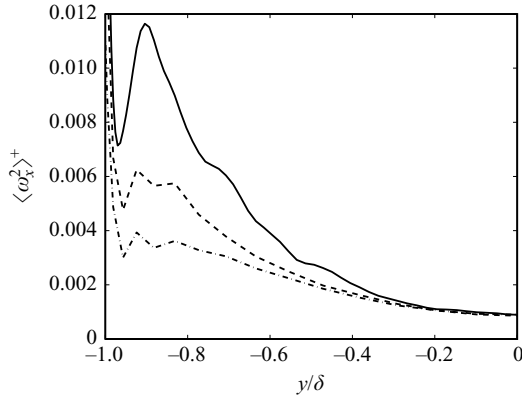


FIGURE 13. Intensity of the streamwise vorticity component in wall units. Filtered DNS is denoted by the solid line, model D by the dashed line and model  $D_{EV}$  by the dash-dotted line.

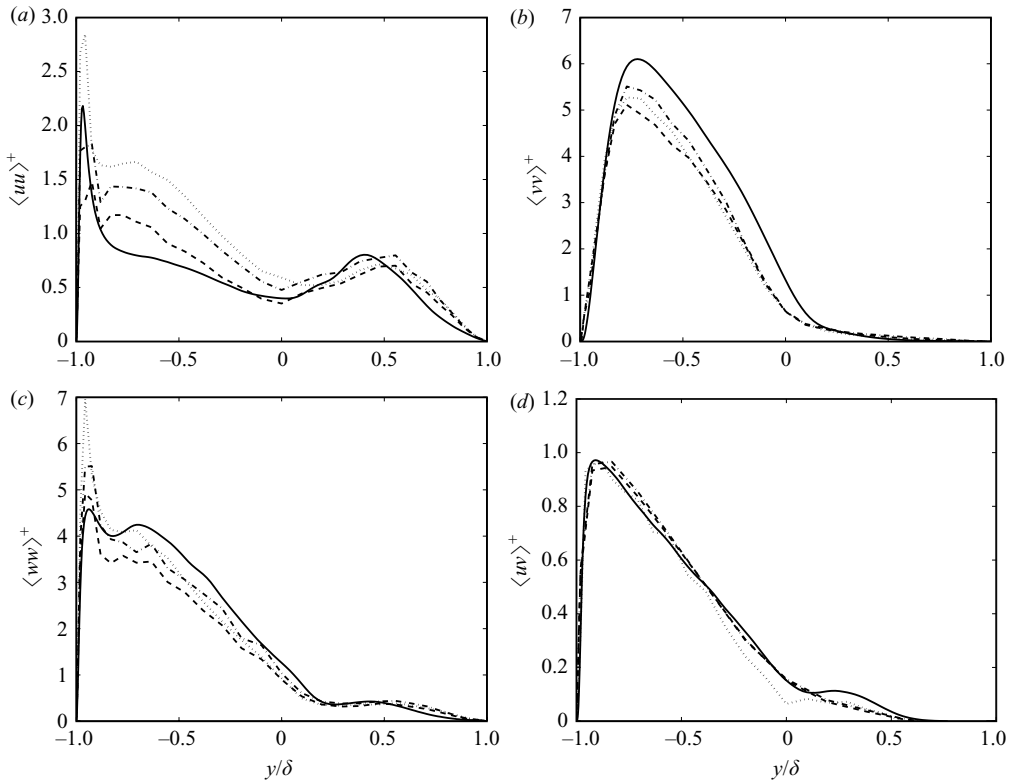


FIGURE 14. Reynolds stresses at  $Ro^+ = 37$ : (a)  $\langle u'u' \rangle^+$ , (b)  $\langle v'v' \rangle^+$ , (c)  $\langle w'w' \rangle^+$  and (d)  $\langle u'v' \rangle^+$ . DNS is denoted by the solid line, model D by the dashed line, model  $D_{EV}$  by the dash-dotted line and model DS by the dotted line.

$D_{EV}$ . Model D improves the Reynolds stresses by reducing  $\langle u'u' \rangle$  at the destabilized side of the channel. Hence, the nonlinear term  $\tilde{S}_{ik}\tilde{\Omega}_{kj} - \tilde{\Omega}_{ik}\tilde{S}_{kj}$  improves the description of the individual Reynolds stresses. At the stable side of the channel the wall-normal stress is almost completely suppressed according to DNS and all models. The  $\langle u'v' \rangle$

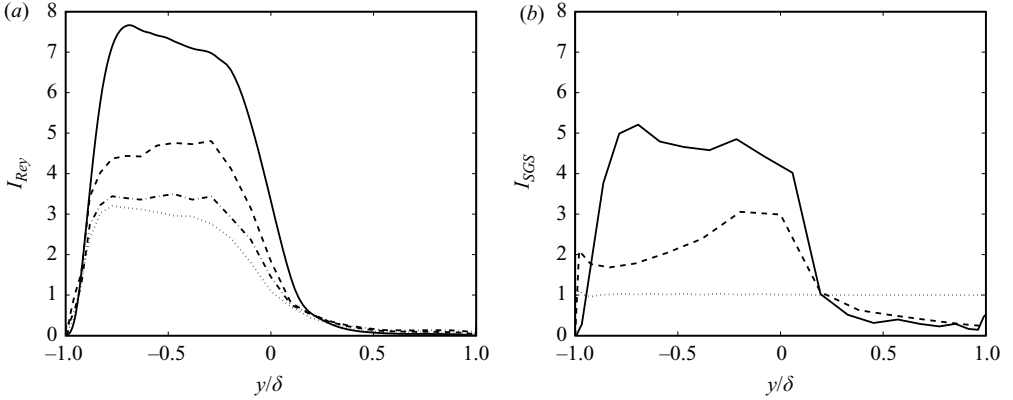


FIGURE 15. (a) Anisotropy ratio of the Reynolds stress and (b) anisotropy ratio of the SGS stress in rotating channel flow at  $Ro^+ = 37$ . DNS is denoted by the solid line, model D by the dashed line, model DS by the dotted line and model  $D_{EV}$  by the dash-dotted line.

stress is accurately captured by both model D and model DS, in consistency with the good prediction of the mean velocity profile.

### 6.3. Anisotropy of the SGS and the SGS dissipation

Figure 15 shows the anisotropy ratios

$$I_{Rey} = \frac{\langle v'v' \rangle}{\langle u'u' \rangle} \quad I_{SGS} = \frac{\langle \tau_{22} \rangle}{\langle \tau_{11} \rangle} \quad (6.4)$$

in the rotating channel where  $I_{Rey}$  describes the anisotropy of the Reynolds stresses and  $I_{SGS}$  describes the anisotropy of the SGS stresses. DNS shows that the large scales are more anisotropic than the SGS with a clear dominance of the wall-normal stress over the streamwise stress at the unstable side of the channel. However, also the SGSs are strongly anisotropic, since  $I_{SGS} \approx 5$  in the core region of the destabilized side of the channel. In figure 15(b) we see that model DS with the trace computed from DNS and model  $D_{EV}$  predict  $I_{SGS} \approx 1$ , i.e. isotropy at the SGS level. Model D gives a higher SGS anisotropy  $I_{SGS} \approx 2.5$  at the destabilized side of the channel, which is in better agreement with DNS. Figure 15(a) shows that also the anisotropy of the Reynolds stress  $I_{Rey}$  is better described. The improved prediction of the individual Reynolds stresses with model D including the nonlinear term are thus due to an improved description of the anisotropy at the SGS level.

The properties of the SGS dissipation are important in LES. Kang & Meneneau (2001) investigated the anisotropy of the SGS dissipation tensor  $\tau_{ij}\tilde{S}_{pq}$  using experimental data. They found that the Smagorinsky model gives a too isotropic SGS dissipation tensor, whereas the nonlinear tensor eddy-viscosity model gives a too anisotropic SGS. Similar to Kang & Meneneau (2001) we compute the SGS dissipation isotropy ratio as

$$I_{22} = \frac{\langle (\tau_{22}\tilde{S}_{22})^2 \rangle}{\langle (\tau_{11}\tilde{S}_{11})^2 \rangle}. \quad (6.5)$$

We only compute  $I_{22}$  using model D and model  $D_{EV}$ . Results for model DS are omitted because there is no easy way to add the trace  $2K_{SGS}$  to  $\tau_{ij}^{Smag}$  in this case. Figure 16 shows that the DNS has a highly anisotropic SGS dissipation with  $I_{22} > 1$  at the destabilized side of the channel and  $I_{22} < 1$  at the stabilized side. Model  $D_{EV}$

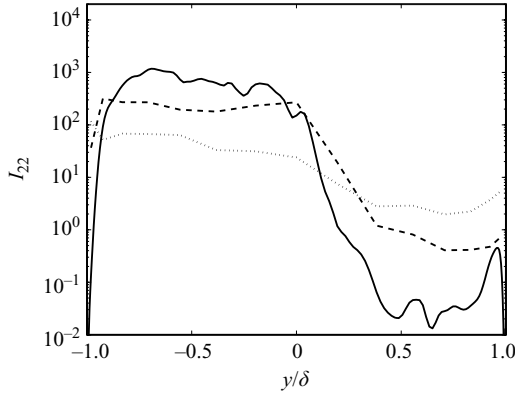


FIGURE 16. Anisotropy of the energy transfer to the SGS in rotating channel flow at  $Ro^+ = 37$ . DNS is denoted by the solid line, model D by the dashed line and model  $D_{EV}$  by the dotted line.

predicts a too isotropic energy transfer, in agreement with the observations of Kang & Meneneau (2001). Model D predicts more anisotropy and is in better agreement with the DNS.

#### 6.4. Tensorial alignment of the SGS stress

The tensorial alignment between the SGS stress and different constituent terms has been examined by several authors, e.g. Horiuti (2001), Tao, Katz & Meneveau (2002) and Wang & Bergstrom (2005). We follow the steps by Wang & Bergstrom (2005) and calculate the averaged angles  $\Lambda_i \in [0^\circ, 90^\circ]$  between the eigenvectors of the negative SGS stress and  $\tilde{S}_{ij}$ . Any eddy-viscosity model has  $\Lambda_i = 0^\circ$  because of the complete alignment between the SGS stress tensor and  $\tilde{S}_{ij}$ . Figure 17 shows the averaged angle between the eigenvectors of the negative SGS stress,  $-\tau_{ij}$ , and the resolved rate of strain,  $\tilde{S}_{ij}$ , corresponding to their largest eigenvalues. According to the filtered DNS,  $\Lambda_1$  is about  $60^\circ$  throughout the channel, indicating that the SGS stress is not aligned with the resolved rate of strain. Model D predicts  $\Lambda_1 \approx 15^\circ$ , which is an improvement over model DS which predicts  $\Lambda_1 = 0$ . However, the angle suggested by the filtered DNS,  $\Lambda_1 = 60^\circ$ , is significantly higher. There can be two reasons. The first reason is that model D only takes into account two constituent terms. A complete description of  $-\tau_{ij}$  would require five terms. The second reason is that the SGS stress computed from DNS includes stochastic noise which is not present in LES. Stochastic noise will increase  $\Lambda_i$ , because it will reduce the alignment between  $-\tau_{ij}$  and  $\tilde{S}_{ij}$ . It is interesting to note that a random vector with a uniformly distributed direction in the upper half-sphere has a mean angle of  $\Lambda \approx 60^\circ$  to the vertical direction. This is very close to the value suggested by DNS.

The angle  $\Lambda_1$  does not change very much with rotation according to the filtered DNS (see figure 17b). There is only a slight tendency of a larger angle at the stabilized side of the channel. We obtain a similar but more pronounced increase for LES with model D (figure 17b).

#### 6.5. Validation in streamwise rotating channel flow

To further investigate the performance of the proposed SGS models we carried out LES of streamwise rotating channel flow at  $Ro^+ = 10$  and  $Re_\tau = 180$  using model D. The LES results were compared to the DNS data by Oberlack *et al.* (2006).

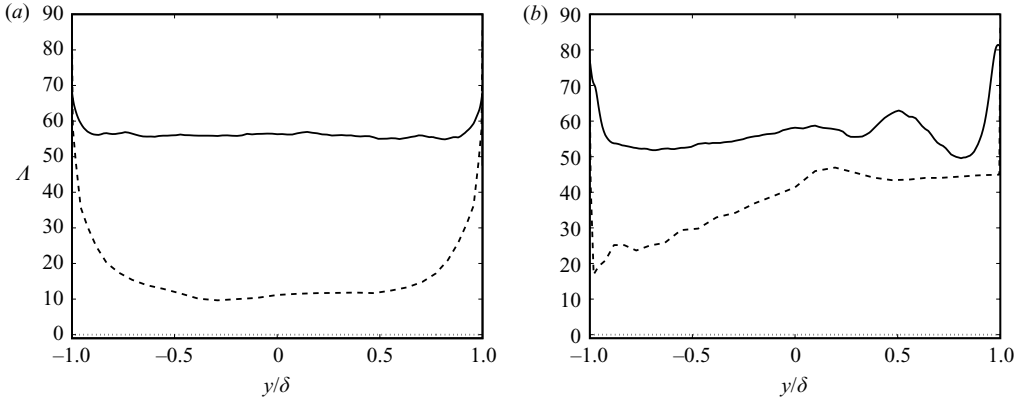


FIGURE 17. Mean angle between the eigenvectors of  $\tilde{S}_{ij}$  and  $-\tau_{ij}$  corresponding to the largest eigenvalues: (a)  $Ro^+ = 0$  and (b)  $Ro^+ = 37$ . DNS is denoted by the solid line, model D by the dashed line and models DS and S by the dotted line.

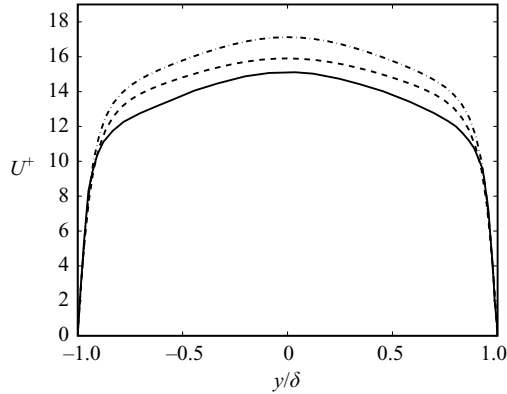


FIGURE 18. Mean streamwise velocity scaled with  $u_\tau$ . DNS is denoted by the solid line, model D by the dashed line and model DS by the dash-dotted line.

The streamwise rotating channel flow is a demanding test case for turbulence models. All Reynolds stress components are non-zero. The  $\langle u'w' \rangle$  component is not produced by mean shear but is induced by the rotation. Oberlack *et al.* (2006) showed that a common Reynolds stress model predicts a  $\langle u'w' \rangle$  component with the wrong sign and cannot capture the reduction of the mean flow rate induced by the rotation. By comparing figures 10(b) and 18, we see that model DS predicts a reduction of the mean flow rate, but the mean streamwise velocity is still much higher than in DNS. Such overprediction of  $U^+$  using the dynamic Smagorinsky model was also observed by Oberlack *et al.* (2006). Although model D also overpredicts  $U^+$  it better captures the reduction of the mean flow rate by the rotation. The shear stresses are well predicted by LES as shown by Oberlack *et al.* (2006), whereas there is less agreement between LES and DNS for the normal stresses. This is seen in figure 19 which shows the resolved streamwise fluctuations. Both model DS and model D overpredict  $\langle u'u' \rangle^+$ , but model D performs significantly better.

$N_x \times N_y \times N_z$	Model DS				Model D			
	$\Delta x^+$	$\Delta y^+$	$\Delta z^+$	$Re_\tau$	$\Delta x^+$	$\Delta y^+$	$\Delta z^+$	$Re_\tau$
$64 \times 97 \times 64$	162	17	81	828	181	19	91	922
$96 \times 97 \times 96$	115	18	52	875	123	20	61	938
$128 \times 129 \times 128$	88	14	44	901	94	15	47	955

TABLE 1. Numerical parameters of the LES:  $N_x$ ,  $N_y$  and  $N_z$  denote the resolution in the streamwise, wall-normal and spanwise directions, respectively.

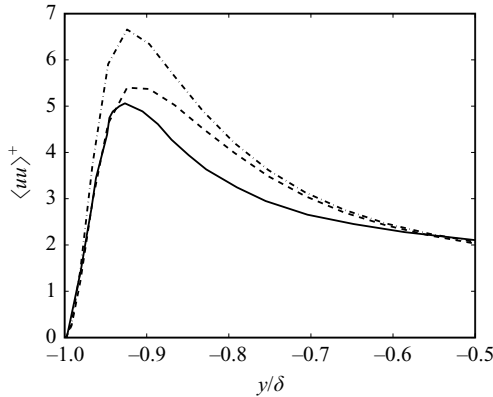


FIGURE 19. Mean resolved streamwise velocity fluctuations scaled with  $u_\tau^2$ . DNS, solid line; model D, dashed line; model DS, dash-dotted line.

## 7. Validation of the explicit algebraic SGS stress model in high-Reynolds-number channel flow

### 7.1. Non-rotating channel flow at various resolution

In order to explore the sensitivity of the models to the grid spacing, we have carried out LES of non-rotating channel flow at  $Re_\tau = 950$  using different resolutions (see § 3). In LES with model D we chose to specify a lower bound of 0.28 for the parameter  $c_1$  in order to avoid too small values near the wall. This value is of the same order as the low-Reynolds-number value of the corresponding parameter in the RANS model developed by Sjögren & Johansson (2000) (see § 5 for a further discussion of this parameter). In the LES the mass flux was fixed in such a way that the bulk Reynolds number was the same as in the DNS by del Álamo *et al.* (2004), in contrast to the other LES in which the pressure gradient was fixed. Table 1 shows the resolution in the LES with models D and DS together with the mean value of  $Re_\tau$ . Note that the resolutions are coarse for LES. The computed value of  $Re_\tau$ , i.e. the wall shear stress, with model DS is significantly lower than the DNS value. LES with model DS at the coarsest resolution underpredicts  $Re_\tau$  by about 13 %, whereas the corresponding value for model D at the same coarse resolution is about 3 %. Hence, LES with model D give values in much better agreement with DNS.

Figure 20 shows the mean velocity profiles. LES with coarsest resolution overpredicts the mean velocity profile in the log layer, but the slope is correctly captured by both models. Model DS predicts a higher normalized mean velocity than model D. The turbulence kinetic energy profiles at the three different resolutions are shown in figure 21(a). Here, we add the subgrid kinetic energy to the resolved

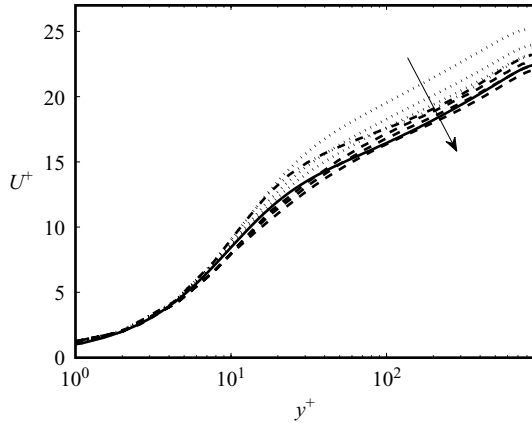


FIGURE 20. Mean velocity profile. DNS (del Álamo *et al.* 2004) is denoted by the solid line, explicit algebraic model D by the dashed lines and model DS by the dotted lines. The arrow points in the direction of increased resolution.

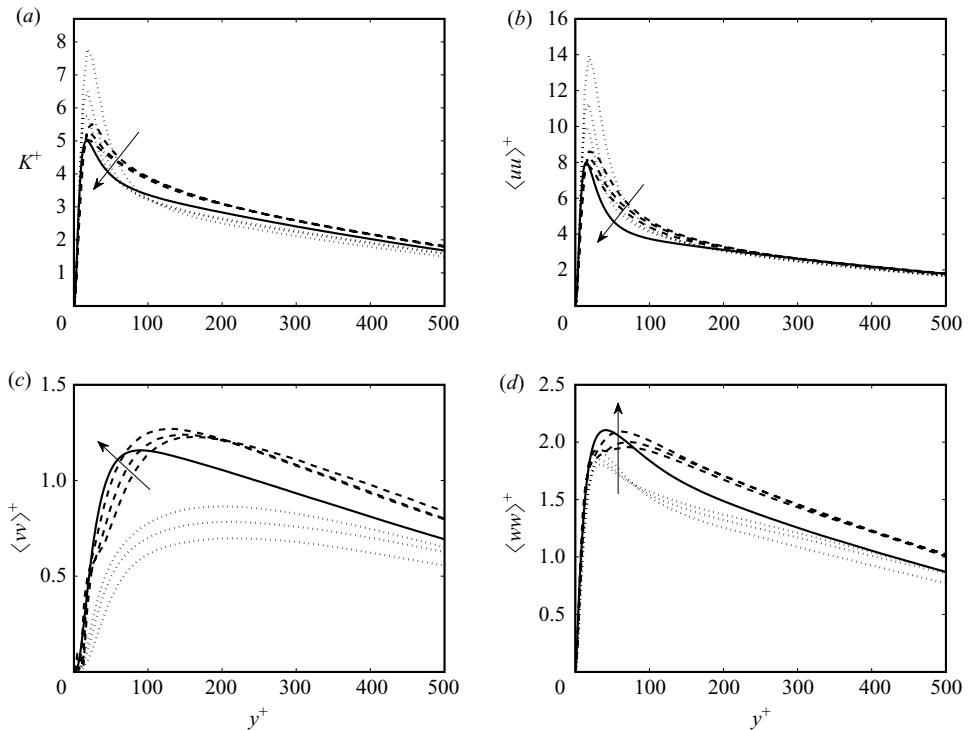


FIGURE 21. (a) Turbulent kinetic energy, (b)  $\langle u'u' \rangle^+$ , (c)  $\langle v'v' \rangle^+$  and (d)  $\langle w'w' \rangle^+$ . DNS (del Álamo *et al.* 2004) is denoted by the solid line, model D by the dashed lines and model DS by the dotted lines. The arrow points in the direction of increasing resolution for model D. For model DS the arrow also indicates the direction of increasing resolution in (a) and (b), but in (c) and (d) it increases in the opposite direction.

kinetic energy when we compare the results of model D and the DNS by del Álamo *et al.* (2004). It is not possible to apply the same procedure to model DS because it does not include a model for the individual diagonal SGS stresses (see Winkelmann, Jeanmart & Carati 2002). Model DS tends to overpredict the near-wall peak in the



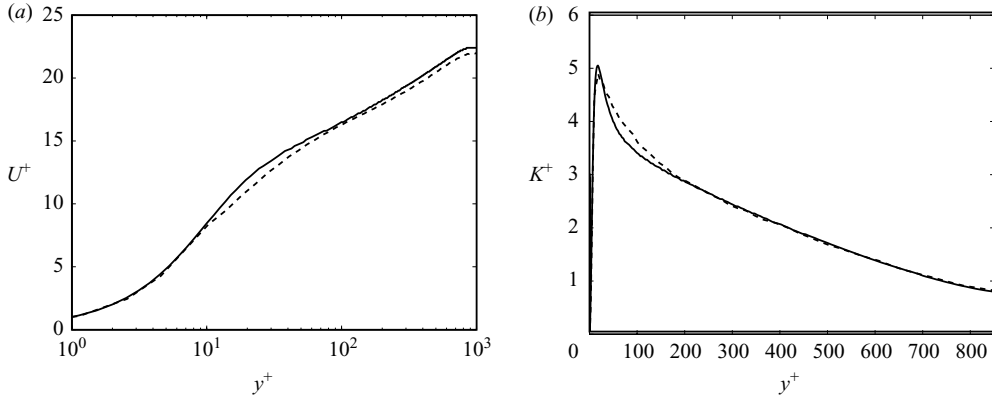


FIGURE 22. Results from LES with  $Ro^+ = 0$  at  $Re_\tau = 950$ . (a) Mean velocity profile. (b) Turbulent kinetic energy. LES is denoted by the dashed line and DNS by the solid line.

resolved kinetic energy, especially at the lowest resolution. It predicts  $\tilde{K} > K$  near the wall, which is incorrect. Moreover the magnitude of the predicted near-wall peak in  $\tilde{K}$  depends strongly on the resolution. Model D provides for a significantly better and less filter-scale-dependent description of  $K$ .

The diagonal Reynolds stresses are shown in figure 21(b)–(d). Again we add the SGS stresses to the resolved Reynolds stresses for the results of model D, whereas the results of model DS are resolved statistics. Model D gives a good and fairly resolution-independent prediction of the diagonal Reynolds stresses, whereas model DS clearly overpredicts the streamwise stress and underpredicts the wall-normal stress. These differences are likely due to the differences in the anisotropy of the SGS dissipation. Near the wall we can expect that the SGS dissipation of the streamwise stress is relatively large, and that of the wall-normal stress is relatively small. Eddy-viscosity models like model DS predict a too isotropic SGS dissipation tensor leading to a too weak and a too strong SGS dissipation of the streamwise and the wall-normal stress, respectively. By including nonlinear terms model D is able to give a better prediction of the SGS dissipation anisotropy as was shown in figure 16. This probably explains the overprediction of the resolved stress anisotropy by model DS and better agreement between model D and the DNS data. The correct prediction of the anisotropy of the SGS dissipation is apparently especially important in LES with coarse resolutions. An overprediction of the near-wall peak in the streamwise fluctuations using model DS also appears in rotating channel flow (see § 6.2).

### 7.2. Spanwise rotation

To investigate the influence of the Reynolds number on rotating channel flow and the performance of the SGS modelling at different Reynolds numbers, we carried out LES at  $Re_\tau = 950$  and compared the results with DNS at  $Re_\tau = 180$ . LESs were represented on  $128 \times 129 \times 128$  grid points and were performed using model D. For the non-rotating case we compared the LES results with the DNS by del Álamo *et al.* (2004), but there are no DNS data available for the rotating cases.

Figure 22 shows the mean velocity profile and the turbulence kinetic energy for LES with  $Ro^+ = 0$ . The mean velocity and turbulence kinetic energy profiles are in good agreement with the DNS data from del Álamo *et al.* (2004) with only a slight overprediction of  $K$  near the wall. These results for  $Ro^+ = 0$  show that the present LES at  $Re_\tau = 950$  gives an accurate prediction. The mean velocity profile and the turbulence kinetic energy for  $Ro^+ = 37$  are shown in figure 23. Results of

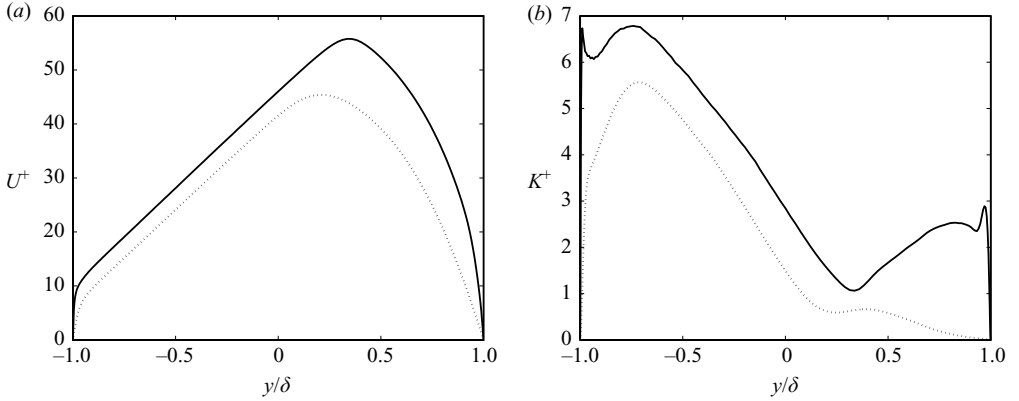


FIGURE 23. Results from LES with  $Ro^+ = 37$  at  $Re_\tau = 950$ . (a) Mean velocity profile. (b) Turbulent kinetic energy. LES is denoted by the solid line and DNS at  $Re_\tau = 180$  by the dotted line.

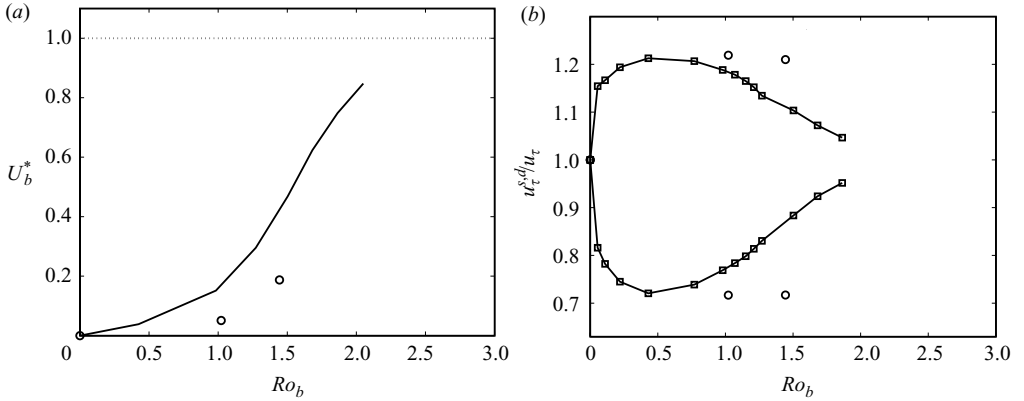


FIGURE 24. (a) Normalized mean bulk velocity and (b) normalized local wall friction velocity  $u_\tau^{d,s}/u_\tau$  at the stabilized and destabilized side of the channel. DNS at  $Re_\tau = 180$  is denoted by  $\square$  and LES at  $Re_\tau = 950$  by  $\circ$ .

LES at  $Re_\tau = 950$  and DNS at  $Re_\tau = 180$  (Grundestam *et al.* 2008) are plotted. In figure 23(a) we see that the region with an approximately constant mean velocity gradient equal to twice the system rotation is slightly larger in LES than in DNS. The scaled turbulent kinetic energy is also affected by the increase in Reynolds number. The fluctuations are more intense at the destabilized side of the channel, and there is no laminarization in LES at  $Ro^+ = 37$  at the stable side (figure 23b). Thus, the increase in Reynolds number seems to delay the laminarization to higher rotation numbers.

The mean bulk velocity defined in (6.3) is shown as a function  $Ro_b$  in figure 24(a). Also here the LES results at  $Re_\tau = 950$  and the DNS results at  $Re_\tau = 180$  are plotted. We normalize  $U_b$  as follows to enable comparison between the two different Reynolds numbers:

$$U_b^* = \frac{U_b - U_b^{non}}{U_b^{lam} - U_b^{non}}, \quad (7.1)$$

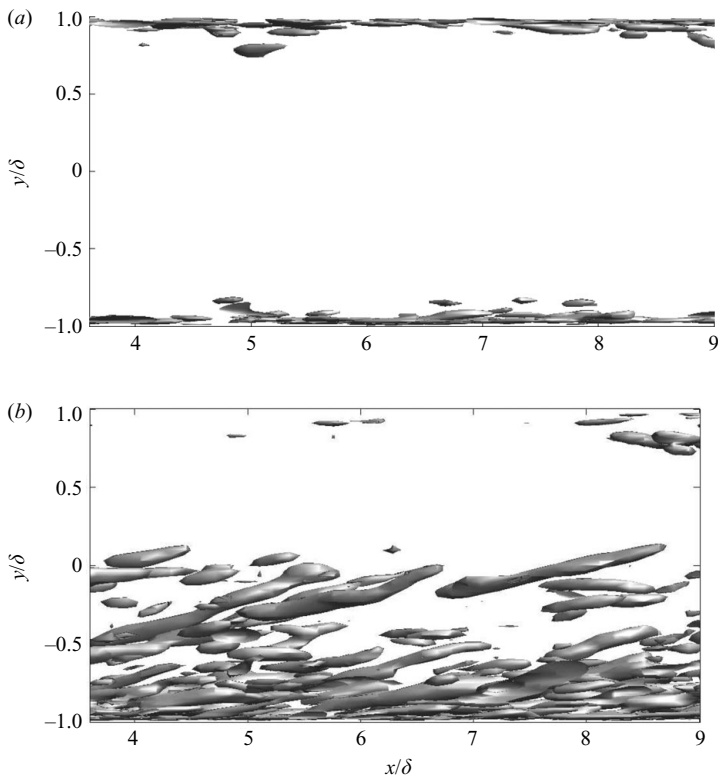


FIGURE 25. Isosurfaces for  $\lambda_2 = -1.7$ : (a)  $Ro^+ = 0$  and (b)  $Ro^+ = 37$ .

where  $U_b^{lam}$  is the bulk velocity for laminar channel flow and  $U_b^{non}$  is the bulk velocity for non-rotating turbulent channel flow. Figure 24(a) shows that  $U_b^*$  increases more slowly with increasing  $Ro_b$  at  $Re_\tau = 950$  than at  $Re_\tau = 180$  according to DNS and LES. However, from stability arguments (see Grundestam *et al.* 2008) one should expect total laminarization to occur at  $Ro_b \leq 3$  independent of the Reynolds number. The variation of the wall friction velocities at both sides of the channel as a function of  $Ro_b$  is shown in figure 24(b). The LES results at  $Re_\tau = 950$  are similar to the DNS results at  $Re_\tau = 180$ . However, there is a tendency of a delayed relaxation towards the laminar value  $u_\tau^{d,s}/u_\tau = 1$  for high  $Ro_b$ . Such delayed laminarization was also found by Alvelius (1999).

Turbulence structures in rotating channel flow have previously been investigated by Lamballais *et al.* (1998). They visualized the vortical structures by isosurfaces of the vorticity field at  $Re_\tau \approx 360$ . In this paper, we visualize the vortical structures in our LES at  $Re_\tau = 950$  using the  $\lambda_2$  visualization method (see Jeong & Hussain 1995). Figure 25 shows isosurfaces for  $\lambda_2 = -1.7$  at  $Ro^+ = 0$  and  $Ro^+ = 37$ . At  $Ro^+ = 0$  we observe only small near-wall structures, whereas we observe tilted large-scale vortical structures at  $Ro^+ = 37$  located at the unstable side of the channel. The structures are very elongated, and some of them reach as far as the stable side of the channel. The local flow conditions at the destabilized side of the channel resemble those of rotating homogeneous shear flow with a rotation rate corresponding to  $2\Omega^s = \partial U/\partial y$ . It is interesting to note that Brethouwer (2005) found coherent elongated vortex tubes in his DNS of rotating homogeneous shear flow at this rotation rate. Lamballais

*et al.* (1998) also observed elongated large-scale vortices at the destabilized side of the channel.

## 8. Conclusions

New explicit SGS stress models involving both the strain rate and rotation rate tensors that account for rotation in a natural way are proposed and validated through LESs of rotating channel flow. Rotating channel flow has proved to be a demanding test case for LES because it involves laminarized regions and highly anisotropic fluctuations. The new models are based on the same methodology that leads to the EARSM formulation for RANS models. Both dynamic and non-dynamic models are proposed. The non-dynamic model is a computationally efficient SGS model which outperforms the standard wall-damped Smagorinsky model in rotating channel flow. The new explicit dynamic model is the most accurate and represents an alternative to the dynamic Smagorinsky model. The model is computationally less expensive than the dynamic Smagorinsky model because it involves fewer test filter operations. The proposed explicit dependence on the system rotation included in both new models improves the description of the mean velocity profile and the turbulent kinetic energy at high rotation rates. Comparison with the dynamic Smagorinsky model shows that the avoidance of the eddy-viscosity assumption improves the description of both the Reynolds stress anisotropy and the SGS stress anisotropy. LESs of non-rotating turbulent channel flow at  $Re_\tau = 950$  show that the new explicit model especially at coarse resolutions significantly better predicts the mean velocity and the wall shear stress than the dynamic Smagorinsky model. The simulated Reynolds stresses with the new model are relatively insensitive to the resolution and agree, even at a coarse resolution, rather well with the DNS data, which is probably the consequence of the improved prediction of the anisotropy of the subgrid dissipation.

LESs of spanwise rotating channel flow at  $Re_\tau = 950$  have also been carried out. The effects of rotation at higher Reynolds numbers are somewhat shifted to higher rotation numbers, although complete laminarization should occur for  $Ro_b \leq 3$  independent of the Reynolds number. Elongated large-scale vortical structures were found at the unstable side of the rotating channel.

We think that the new models have potential for LES of rotating and wall-bounded flows. Since the new subgrid models have strong similarities with the EARSM they might also have promising features for detached-eddy simulations.

Fruitful discussions on this topic with Dr Stefan Wallin are gratefully acknowledged. We also want to thank Dr P. Schlatter for providing the DNS data at  $Re_\tau = 180$  and Peter Lenaers and Amin Rasam for carrying out some simulations. The project was funded by the Swedish Research Council. Computer time was provided by Swedish National Infrastructure for Computing (SNIC).

## Appendix. Pressure-strain modelling

The model for the rapid part of  $\Pi_{ij}$  is very similar to its RANS counterpart. It only differs from the original model in the coefficient in front of  $\tilde{S}_{ij}$ . In order to investigate if the model is reasonable we perform an *a priori* test at  $\Delta_x^+ = 47$ ,  $\Delta_z^+ = 24$  which is a typical resolution for LES. From figure 26 we can see that the rapid model captures the behaviour of  $\langle \Pi_{12} \rangle$  fairly well and the behaviour of  $\langle \Pi_{11} \rangle$  in a qualitative way.

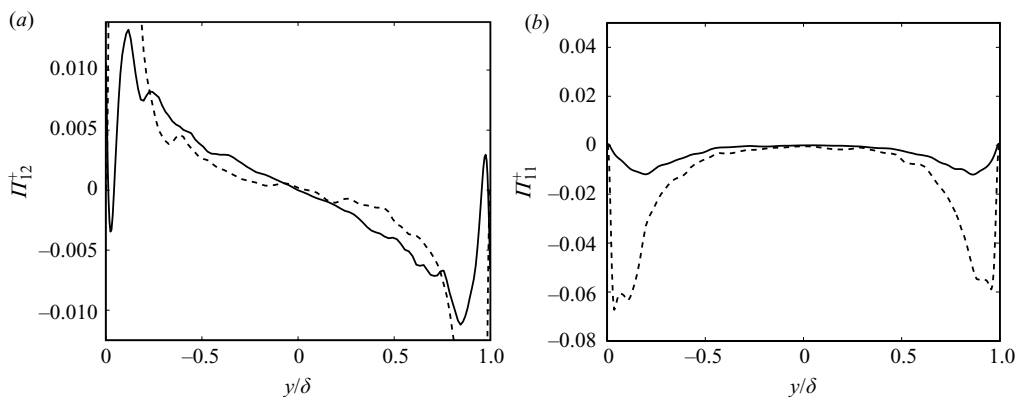


FIGURE 26. Validation of the model for the SGS pressure strain,  $\langle \Pi_{ij} \rangle$ . (a)  $\langle \Pi_{12} \rangle$  and (b)  $\langle \Pi_{11} \rangle$ . Filtered DNS, solid line; model, dotted line.

Hence, the model is reasonable in the mean sense, and we believe that there is no clear reason to construct a more complicated model.

#### REFERENCES

- DEL ÁLAMO, J. C., JIMÉNEZ, J., ZANDONADE, P. & MOSER, R. D. 2004 Scaling of the energy spectra of turbulent channels. *J. Fluid Mech.* **500**, 135–144.
- ALVELIUS, K. 1999 Studies of turbulence and its modelling through large eddy and direct numerical simulation. PhD thesis, Department of Mechanics, KTH, Sweden.
- BARDINA, J., FERZIGER, J. H. & REYNOLDS, W. C. 1983 Improved turbulence models based on large eddy simulation of homogeneous incompressible flow. *Tech Rep.* TF-19, Stanford University.
- BRETHOUWER, G. 2005 The effect of rotation on rapidly sheared homogeneous turbulence and passive scalar transport: linear theory and direct numerical simulations. *J. Fluid Mech.* **542**, 305–342.
- CHEVALIER, M., SCHLATTER, P., LUNDBLADH, A. & HENNINGSON, D. S. 2007 SIMPSON—a pseudo-spectral solver for incompressible boundary layer flows. *Tech Rep.* TRITA MEK 2007:07. KTH.
- CLARK, R. A., FERZIGER, J. H. & REYNOLDS, W. C. 1979 Evaluation of subgrid-scale models using an accurately simulated turbulent flow. *J. Fluid Mech.* **91**, 1–16.
- FUREBY, C. & TABOR, G. 1997 Mathematical and physical constraints on large-eddy simulations. *Theoret. Comput. Fluid Dyn.* **9**, 85–102.
- GATSKI, T. B. & WALLIN, S. 2004 Extending the weak-equilibrium condition for algebraic Reynolds stress models to rotating and curved flows. *J. Fluid Mech.* **518**, 147–155.
- GERMANO, M. 1992 Turbulence: the filtering approach. *J. Fluid Mech.* **238**, 325–336.
- GHOSAL, S., LUND, T. S., MOIN, P. & AKSELVOLL, K. 1995 A dynamic localization model for large-eddy simulation of turbulent flows. *J. Fluid Mech.* **286**, 229–255.
- GRUNDESTAM, O., WALLIN, S. & JOHANSSON, A. V. 2008 Direct numerical simulations of rotating turbulent channel flow. *J. Fluid Mech.* **598**, 177–199.
- HORIUTI, K. 2002 Alignment of eigenvectors for strain rate and subgrid-scale stress tensors. In *Direct and Large-Eddy Simulation IV* (B. J. Geurts, R. Friedrich, O. Métais) ERCOFTAC Series 8, pp. 67–72. Kluwer.
- JEONG, J. & HUSSAIN, F. 1995 On the identification of a vortex. *J. Fluid Mech.* **285**, 69–94.
- KANG, H. S. & MENEVEAU, C. 2001 Passive scalar anisotropy in a heated turbulent wake: new observations and implications for large eddy simulations. *J. Fluid Mech.* **442**, 161–170.
- KOSOVIĆ, B. 1997 Subgrid-scale stress modelling for the large-eddy simulation of high-Reynolds-number boundary layers. *J. Fluid Mech.* **336**, 151–182.
- KRISTOFFERSEN, R. & ANDERSSON, H. I. 1993 Direct simulations of low-Reynolds-number turbulent flow in a rotating channel. *J. Fluid Mech.* **256**, 163–197.

- LAMBALLAIS, E., MÉTAIS, O. & LESIEUR, M. 1998 Spectral-dynamic model for large-eddy simulations of turbulent rotating channel flow. *Theoret. Comput. Fluid Dyn.* **12**, 149–177.
- LAUNDER, B. E., REECE, G. J. & RODI, W. 1975 Progress in the development of a Reynolds-stress turbulence closure. *J. Fluid Mech.* **68**, 537–566.
- LILLY, D. K. 1992 A proposed modification of the Germano subgrid scale closure method. *Phys. Fluids A* **4**, 633–635.
- LUND, T. S. & NOVIKOV, E. A. 1992 Parameterization of subgrid-scale stress by the velocity gradient tensor. In *Annual Research Briefs*, pp. 27–43. Center for Turbulence Research, NASA Ames.
- MARSTORP, L., BRETHOUWER, G. & JOHANSSON, A. V. 2007 A stochastic subgrid model with application to turbulent flow and scalar mixing. *Phys. Fluids* **19**, 035107.
- MENEVEAU, C., LUND, T. S. & MOIN, P. 1992 Search for subgrid scale parametrization by projection pursuit regression. In *Proceedings of Summer Program*, pp. 61–81. Center for Turbulence Research, NASA Ames.
- OBERLACK, M., CABOT, W., PETERSON REIF, B. A. & WELLER, T. 2006 Group analysis, direct numerical simulation and modelling of a turbulent channel flow with streamwise rotation. *J. Fluid Mech.* **562**, 383–403.
- POPE, S. B. 2000 *Turbulent Flows*. Cambridge University Press.
- SCHLATTER, P., STOLZ, S. & KLEISER, L. 2004 LES of transitional flows using the approximate deconvolution model. *Intl J. Heat Fluid Flow* **25**, 549–558.
- SJÖGREN, T. & JOHANSSON, A. V. 2000 Development and calibration of algebraic nonlinear models for terms in the Reynolds stress transport equations. *Phys. Fluids* **12**, 1554–1572.
- SPEZIALE, C. G. 1985 Subgrid scale stress models for the large-eddy simulation of rotating turbulent flows. *Geophys. Astrophys. Fluid Dyn.* **33**, 199–222.
- TAO, B., KATZ, J. & MENEVEAU, C. 2002 Statistical geometry of subgrid-scale stresses determined from holographic particle image velocimetry measurements. *J. Fluid Mech.* **457**, 35–78.
- TSUBOKURA, M., KOBAYASHI, T., TANIGUCHI, N. & KOGAKI, T. 1999 Subgrid scale modelling for turbulence in rotating reference frames. *J. Wind Engng Ind. Aerodyn.* **81**, 361–375.
- VREMAN, B., GEURTS, B. & KUERTEN, H. 1994 On the formulation of the dynamic mixed subgrid-scale model. *Phys. Fluids* **6**, 4057–4059.
- WALLIN, S. & JOHANSSON, A. V. 2000 An explicit algebraic Reynolds stress model for incompressible and compressible turbulent flows. *J. Fluid Mech.* **403**, 89–132.
- WANG, B. C. & BERGSTROM, D. J. 2005 A dynamic nonlinear subgrid-scale stress model. *Phys. Fluids* **17**, 035109.
- WINCKELMANS, G. S., JEANMART, H. & CARATI, D. 2002 On the comparison of turbulence intensities from large-eddy simulation with those from experiment or direct numerical simulation. *Phys. Fluids* **14**, 1809–1811.
- WONG, V. C. 1992 A proposed statistical-dynamic closure method for the linear or nonlinear subgrid-scale stresses. *Phys. Fluids A* **4**, 1080–1082.